

Long-period and volcano-tectonic earthquakes record cycles of opening and closing in the enhanced seismic catalog of the 2008 Okmok Volcano, Alaska, eruption

Ricardo Garza Giron¹, Emily E. Brodsky¹, Zack J. Spica¹, and Peter W. Webley¹

¹Affiliation not available

April 16, 2023

Introduction

The degree of openness of a volcanic system is recognized as a major determinant of behavior (e.g., Vergnolle & Métrich, 2021; Seropian et al., 2021; Roman et al., 2019). Whether magma or gas can escape determines the state of stress, and ultimately the eruptibility. Similarly, when an eruption begins, the opening of the vent is the most important factor in any subsequent dynamics. Eruptions are often prolonged and complex sequences of events with eruptive plumes separated by quiescent periods, that might be indicative of resealing, changes in magma fragmentation, or exhaustion of supply. Characterizing the eruptive processes is difficult as high temporal resolution of co-eruptive observations requires techniques that can track behavior continuously during one of the most difficult-to-observe periods of the volcanic cycle.

Volcano seismicity provides a promising road into solving the problem since often the earthquake record provides continuous and highly resolved information. However, seismicity during long-lived, explosive eruptions is practically invisible because of the extreme noise levels of the eruption itself. In a companion paper, we have set out a workflow to solve the detection problem utilizing modern earthquake detection methods (Garza-Giron et al., submitted). As we showed in that paper, we can use a combination of traditional, machine learning and template matching approaches to expand the co-eruptive seismic catalog of the 2008 Okmok Volcano eruption by about a factor of 10. In this paper we now use that catalog to address the first-order questions about co-eruptive seismicity that have not been previously accessible: *When does the overall earthquake rate increase or decrease in context of the eruption? How does the seismicity evolve as the volcano opens and reopens to erupt material?*

Okmok Volcano is a 10 km wide basaltic-andesitic caldera located on Umnak Island, in the Aleutian arc of Alaska (Figure 1). For over a century, most of the eruptions, the last of which occurred in 1997, had their source at an intra-caldera cone (Cone A; Figure 1 inset) and were mostly Hawaiian to Strombolian (Coats, 1950; Grey, 2003). The 12 July 2008 eruption, which was given a scale of 4 in the Volcanic Explosivity Index (VEI), marked a change in this behavior because of the interactions between magma and water, making new intra-caldera maars and developing a new tephra cone during a large phreato-magmatic eruption (Larsen et al., 2015). Since the island has a topographical regional-scale tilt toward the northeast, the northern sector is characterized by larger bodies of surface and groundwater, with approximately 10^{10} kg of water available for the 2008 eruption (Unema et al., 2016). Multiple geophysical studies, most of which focused on modeling the source of geodetic deformation, have found the location of a shallow (2-4 km) magma reservoir at approximately the same location in the caldera (Figure 1; Mann et al., 2002; Fournier et al., 2009; Biggs et al., 2010; Freymueller and Kaufman, 2010; Lu and Dzurisin, 2010; Masterlark et al., 2010; Albright et al., 2019; Xue et al., 2020; Wang et al., 2021). Furthermore, different authors have shown that inflation cycles

started immediately after the end of the deflationary eruptive periods in 1997 and 2008, suggesting a quick replenishment of the shallow magma reservoir to compensate the pressure gradient (Lu et al., 2005; Lu and Dzurisin, 2010; Freymueller and Kaufman (2010); Wang et al., 2021).

During the 6 months preceding the eruption, the Alaska Volcano Observatory (AVO) detected only 9 low magnitude ($M \leq 2.6$) earthquakes, although many of the stations in the region had outages during those months. Most of the inter-eruptive seismicity is localized in a geothermal field on the isthmus of Umnak Island inland from Inanudak Bay (Figure 1). The only precursory activity to the eruption came on 12 July 2008, when the seismic network at Okmok Volcano recorded the onset of a ~ 4.5 hour-long earthquake swarm (Larsen et al., 2009; Johnson et al., 2010) after which explosive activity commenced. The short sequence of precursory earthquakes was reanalyzed by Ohlendorf et al. (2014) using the AVO catalog, and the earthquakes originated at approximately 3 km depth beneath the intra-caldera cone known as Cone D (Figure 1 inset). The beginning of the eruption was marked by a large-scale sub-Plinian explosion that released a ~ 16 km above sea level (ASL) high dark plume, consistent with a VEI 4 eruption (Newhall and Self, 1982). This plume was accompanied by more than 12 hours of continuous high-amplitude seismic eruption tremor (Larsen et al., 2009). Tremor continued at variable levels throughout the 40-day-long eruption and emanated mainly from a new intra-caldera cone (Haney, 2010; Haney, 2014). This new cone, to the north of Cone D and built during the 2008 eruption, was subsequently named Ahmanilix, which means ‘surprise’ in the language of the Unangan people whose ancestral lands included Umnak Island (Larsen et al., 2015). After the initial plume, the activity continued by the opening, and perhaps widening, of new vents in a westward alignment from the north-west of Cone D. On July 19, the network recorded high-amplitude continuous tremor that lasted ~ 20 hours, and is thought to be related to the initiation of the temporary drainage of the perennial North Cone D Lake (hereby called North Lake) (Figure 1). The drainage of the lake was verified by satellite imagery until August 1 when standing water was observed again at the lake (Larsen et al., 2015). Whether the lake refilled before August 1 is unknown. Moreover, Larsen et al. (2015) reported that between July 24 and August 1 the North Vent structure, directly to the north of Ahmanilix, widened and there was an increase in number and size of reflectors observed in Synthetic Aperture Radar (SAR) images, accompanied by an increase in ash production from August 1 until August 3, confirmed by AVO staff in the field. From August 3 until August 19, when the last emission of ash was reported and the eruption officially ended, the plumes decreased in number and size.

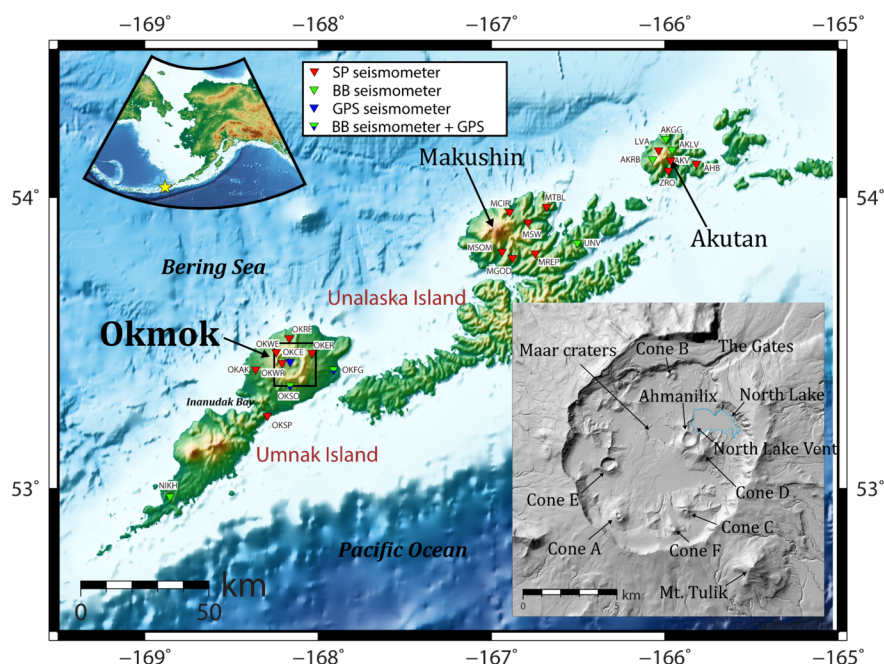


Figure 1. Map of the study region . Stations (red: short-period seismometer; green: broadband seismometer; blue: GPS) used for this study with an inset showing the location of the intra-caldera cones and the most important features of Okmok Volcano. Inset corresponds to black rectangle in the larger map.

Here, we provide a detailed seismological perspective of the eruption by analyzing the enhanced earthquake catalog. After briefly describing the methods of measuring seismicity rate, clustering and magnitude distribution, we present the resultant rates of both LP and VT earthquakes. The two types of earthquakes show distinct trends with the LPs clustering around the eruptive plumes, likely indicating a period of clogging and overpressure, and the VTs continuing steadily during the eruption, likely as result of the pervasive stresses in the solid edifice. The distinction continues through the final closing sequence of the eruption. The only notable exception is the initial opening sequence, as we will discuss below. Ultimately we conclude that LP earthquake rates are highest in clogged periods when there is no eruptive plume and lowest when the vent is cracked open and discharging, while VT earthquakes reflect the stressing regime primarily through their b -values rather than their locations and timing.

Data and methods

We discuss the creation of the enhanced seismic catalog in our complementary paper (Garza-Giron et al., submitted). This high-resolution catalog was built using multiple earthquake detection algorithms in tandem. Two machine learning algorithms and the original analyst catalogs were combined to form a library of templates that were then used to expand the catalog further. Locations for the catalog were determined and then the relative relocations were found using two different algorithms: hypoDD and GrowClust (Waldhauser and Ellsworth, 2000; Trugman and Shearer, 2017). Once locations were determined, consistent local magnitudes were estimated using a local attenuation relationship. Finally, the catalog was divided into two classes of events based on their spectral content: high-frequency volcano-tectonic events (VT) and long-period events (LP). VTs show most of their power above 5 Hz, while the LPs have most of their energy below the 5 Hz threshold. Further details, including a discussion of uncertainties, are available in Garza-Giron et al., submitted).

There are a total number of 3,101 earthquakes in the catalog, 3,041 of which have a magnitude estimation, 2,089 were successfully relocated by hypoDD, and 1,398 were relocated by GrowClust. For the analysis of this paper, we have selected events that were located using a minimum of five stations (1,334 for hypoDD and 983 for GrowClust). We use the catalog relocated with hypoDD, which permitted more relocations than GrowClust, and we compare the two different relocation catalogs when appropriate to guarantee the robustness of the observations. All the interpretations derive from observations that are present in both relocated catalogs as illustrated in the Supporting Information (Figures S1-S4).

Earthquake rates

One of the key questions of this study is: *When does the overall earthquake rate increase or decrease in context of the overall eruption?* The detection methods deployed allow us to ask these questions even during the high noise levels of the eruption. However, noise levels may fluctuate; thus, comparing the observable seismicity rate over time requires a correction for variable detection levels due to noise.

Therefore, we calculate seismicity rate separately for the three different stages of eruption: pre-eruptive, co-eruptive and post-eruptive. For each period, we compute the completeness magnitude using the maximum curvature method plus a correction of 0.1 to compensate for the common underestimation of M_c (Wiemer and Wyss, 2000). Magnitudes were rounded to two significant figures (i.e. $\Delta M = 0.01$). We count the events above M_c using moving time windows of different sizes to estimate the observable seismicity rate. In choosing different time windows, we are effectively applying a low-pass filter to the seismicity rate sequence and different periods will give information at different temporal resolutions. Therefore, we present a long-period trend (earthquakes every 48 hours) to show a global perspective of the rates during the whole eruptive

process and we also provide a highly sampled rate (earthquakes every 4 hours) to analyze the behavior of VT and LP earthquakes in detail during the most critical stages of the eruption.

Earthquake clustering

The cross-correlation of volcanic earthquakes to detect earthquake clusters or multiplets is common practice in studying volcanic processes (e.g., Buurman et al., 2006; Petersen, 2007; Umakoshi et al., 2008; Thelen et al., 2011). In this paper, we use this technique not to find multiplets or families of earthquakes but rather to create more insight into the dynamics of the eruptive process at Okmok Volcano. Our method is as follows: 3 seconds of the waveforms of each event in all available stations (0.2 s before P- 2.8 s after P) is analyzed with all waveforms processed by removing the mean, applying a linear detrending and a 5% Hanning window taper and filtered between 3 - 10 Hz. Using these waveforms, we create a cross-correlation matrix based on the average cross-correlation across all synchronous stations for each pair of events. The matrix distinguishes the events that are well-correlated and thus quantitatively support the existence of bursts.

Magnitude distributions

Variations in magnitude distributions are captured by variations in the b -value of the Gutenberg-Richter distributions where the number of earthquakes of magnitude greater than or equal to M is proportional to 10^{-bM} . The b -value is most commonly estimated with a maximum likelihood estimator that requires knowledge of the minimum magnitude at which the detection level is near 100% (Aki, 1965; Utsu, 1965). This sensitivity to the completeness level is problematic for the Okmok Volcano data, where noise level is constantly changing. Therefore, we utilize the b^+ -positive (b^+) method recently introduced by van der Elst (2021) that uses the inter-event magnitude differences, which follow a distribution of the same functional form as Gutenberg-Richter. As can be seen from the positive differences distributions (Figure S5), the major advantage of the b^+ estimate is that it provides robust measurements of b -values without explicitly requiring an estimate of the completeness magnitude. It is not as strongly biased by its value as the maximum likelihood procedure. We calculated the uncertainty of each b^+ measurement by bootstrapping the magnitude difference distribution 300 times.

The b -value variations require a significance test. Since the distribution of the differences in magnitudes has the same mathematical form as the distribution of the magnitudes (van der Elst, 2021), we calculated the probability that two different b^+ values come from the same populations using the Utsu test (Gerstenberger et al., 2001; Schorlemmer et al., 2005; and references thereafter) to establish the statistical significance of our results. This test was derived for the commonly used b -value, and the resulting probability P of randomly obtaining the observed result is

$$P \approx e^{(\frac{-dA}{2}-2)}, \quad (1)$$

and the parameter dA is defined by

$$dA = -2N \ln(N) + 2N_1 \ln(N_1 + N_2 b_1/b_2) + 2N_2 \ln(N_2 + N_1 b_2/b_1) - 2, \quad (2)$$

where N_1 , b_1 and N_2 , b_2 are the number of events and b values in groups 1 and 2, respectively, and the total number of events is N , which is equal to $N_1 + N_2$.

Results: The sequence of the eruption as shown by the enhanced catalog

Figure 2 presents an overview of the co-eruptive VT and LP magnitudes in context of the major eruptive events as recorded by the deformation, seismic noise and narrative data. There is a notable lack of low magnitude VT and LP events recorded during the eruption that correlates with an increase in the 1-5 Hz

Real-time Seismic Amplitude (RSAM) (i.e., tremor noise level; Figure 2a). Interestingly, the change in magnitude of completeness before, during and after the eruption matches almost exactly the sequence of earthquakes observed for the 2021 eruption in La Palma, Canary Islands (see Figure 7a of D’Auria et al., 2021). The RSAM shown here is the root-mean-square (RMS) seismic amplitude in 5 minute windows, averaged across the two broadband stations (OKFG, OKSO). The drop in RSAM at the end of the eruption seen in Figure 2 corresponds to the improved detection of small earthquakes (Figure 2) as well as the reduced magnitude of completeness after the eruption (Figures S6 and S7).

The high co-eruptive tremor noise level justifies the specialized methods required in this study. These methods have detected nearly an order of magnitude more events than originally recorded (black data points in Figure 2a), but do not completely solve the problem that the detection of small events is challenging during an eruption. Nonetheless, as will be discussed below, the improved catalog not only illustrates seismicity rate changes and changes in magnitude distributions that help understand the open and closed dynamics of the 2008 eruption, but it also illuminates the structure of the volcano with outstanding resolution. To put it into perspective, the number of earthquakes detected and located during the 1.5 months period of the eruption (3,101) is comparable to the total number of earthquakes reported in the catalog from 2001 to 2018 (3,002; Power et al., 2019), and the earthquakes relocated with hypoDD (2,898) represent ~99.56% of the earthquakes in the catalog.

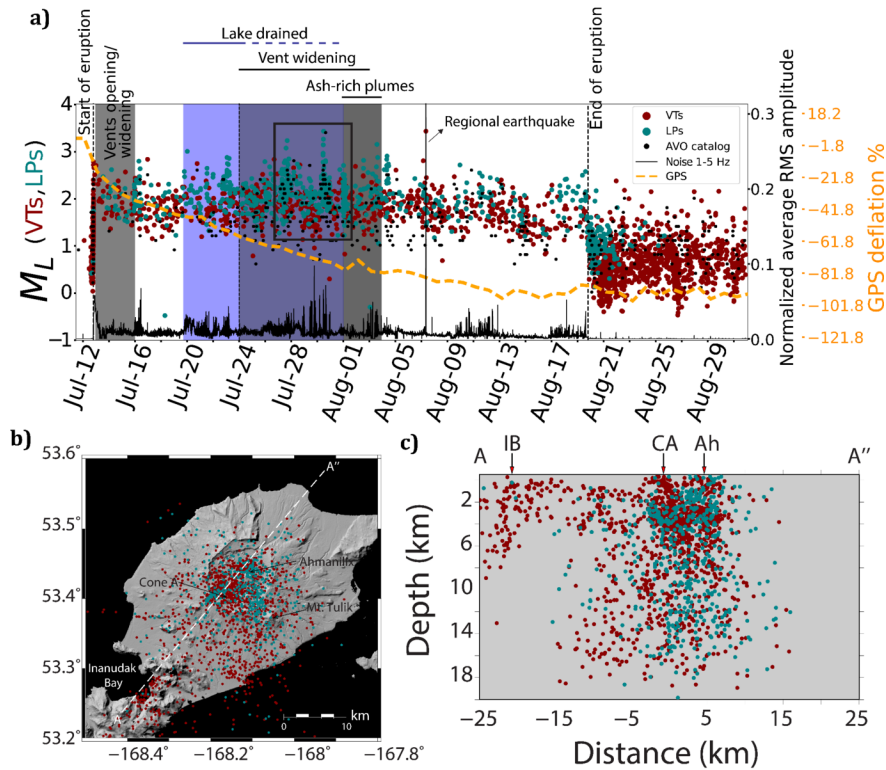


Figure 2. Overview of earthquake catalog and chronology . a) Magnitude of all earthquakes separated by their classification (VTs=red, LPs = turquoise) and contextual deflation, seismic amplitude and narrative data. The deflation rate is derived from GPS by Freymueller and Kaufman (2010) (orange dashed curve, right-hand axis in matching color). Shaded background and annotation indicate major periods in the eruption chronology of Larsen et al. (2010). Black rectangle indicates the interval of bursts of migrating LPs discussed in text. The black line is the average RMS amplitudes in the two broadband stations (OKFG and OKSO) at 1-5 Hz measured every 5 minutes. The large spike in RSAM on August 7 corresponds to a regional earthquake

that was picked up by the network. *b)* Map and *c)* cross-sectional view of the relocated VTs (red) and LPs (turquoise). Width of cross-section = 4 km; azimuth = 40°. Arrows: IB=Inanudak Bay; A=Cone A; Ah=Ahmanilix.

A first inspection reveals patterns in the enhanced catalog that mimic the observational chronology of the eruption from Larsen et al. (2015) (shaded areas) and the GPS data from Freymueller and Kaufman (2010) (Figure 2). For example, the first burst of LP events occurs right after the initial phase of vents opening/widening (July 16), after which there is a change in the slope of the GPS decay at OKFG. Also, the most notable increase in LP activity is during the middle of the eruption (black box in Figure 2a) and it matches well with the periods when Larsen et al. (2015) observed further widening of the North vent (see Figure 1 for location), and the largest bursts occur before, during and after a period of increased ash content observed in the eruptive plumes. The GPS curves represent the time series of the radial displacements detrended and normalized using the quiescence period between 2005 and 2008, so 0% GPS inflation represents the value at the beginning of 2008 (Freymueller and Kaufman, 2010). Assuming a stationary deflation source, the GPS indicates that the caldera subsurface was slightly inflated at the onset of the eruption and it generally deflated rapidly during the eruption before slowing down during the final sequence.

Most of the seismicity leading up to the eruption is tightly clustered underneath the area where the main eruptive vents formed and almost all of the earthquakes were classified as VTs (Figure 3a). The co-eruptive seismicity is essentially localized in and around the volcano's caldera in a bowl-shaped volume (Figure 3b). This population includes LP events that are well-clustered near the active vents, as well as near Cone A, and VTs that are more broadly distributed but are also sporadically clustered near Cone A. Finally, most of the seismicity after the last plume emission is located in the southern sector of the caldera near Cone A (Figure 3c).

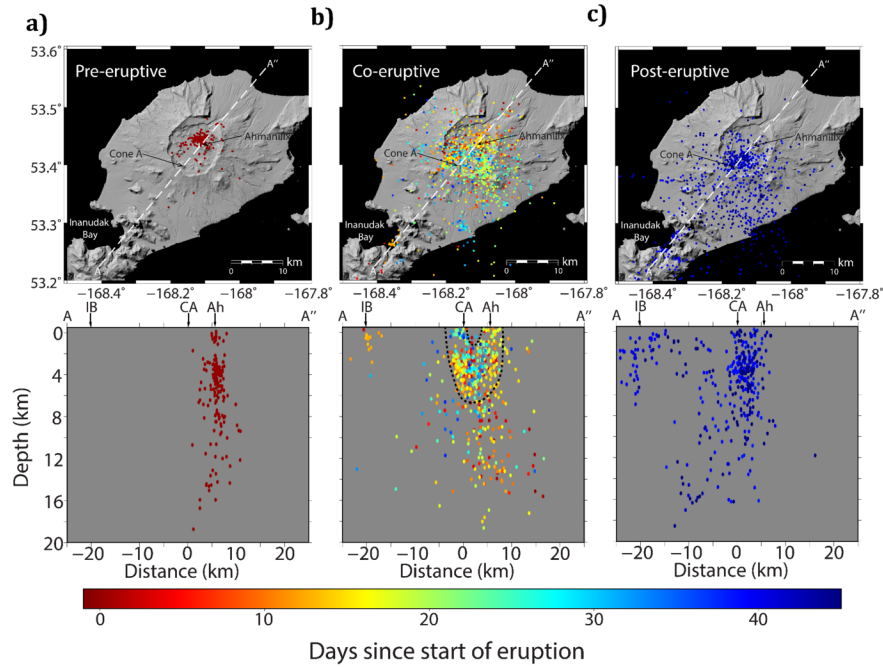


Figure 3. *HypoDD relocated events before (a), during (b) and after (c) the eruption . The sequence leading up to the eruption clusters underneath the vents that developed during the eruption. The co-eruptive seismicity shows a bowl-shaped volume (dashed line) inside the caldera with most of the activity occurring under Cone A and Ahmanilix. The post-eruptive sequence has earthquakes in the south sector of the caldera primarily in the vicinity of Cone A. Cross sectional width = 3 km/azimuth = 40°. Arrows:*

Ah=*Ahmanilix*; *CA*=*Cone A*; *IB*=*Inanudak Bay*.

Reassured by the general correspondence of the chronology, we now move onto a systematic comparison of the relationship of the LPs and VTs to the eruptive events and the relationship of the seismicity as a whole to the structure of the volcano. We separate our findings into six key observations:

Observation 1: Co-eruptive long-period (LP) earthquakes related to venting processes and volcano-tectonic (VT) events independent of plumes

Seismicity rate indicates the difference between LPs and VTs.

To understand how seismicity relates to the eruptive processes, we measured a long period (48-hour) and high-temporal resolution (4-hour) seismicity rate for the VT and LP populations and compared the time series to the reported plume heights (Larsen et al., 2009) and GPS time series data (Figure 4).

To ensure the accuracy of the timing of the plume height data during the middle of the eruption, we cross-check the times against Advanced Very High Resolution Radiometer (AVHRR) satellite observations (Figure S8). If there were plumes reported during times when the satellite imagery does not show any evidence of emissions (red frames in Figure S8) we removed the reported plumes from the data set. There is one time period, however, when emissions are clearly observed in the satellite images but no plumes were reported (July 31 12:30 - July 31 21:30), we mark this time period with a dashed green box in Figures 4 and 5.

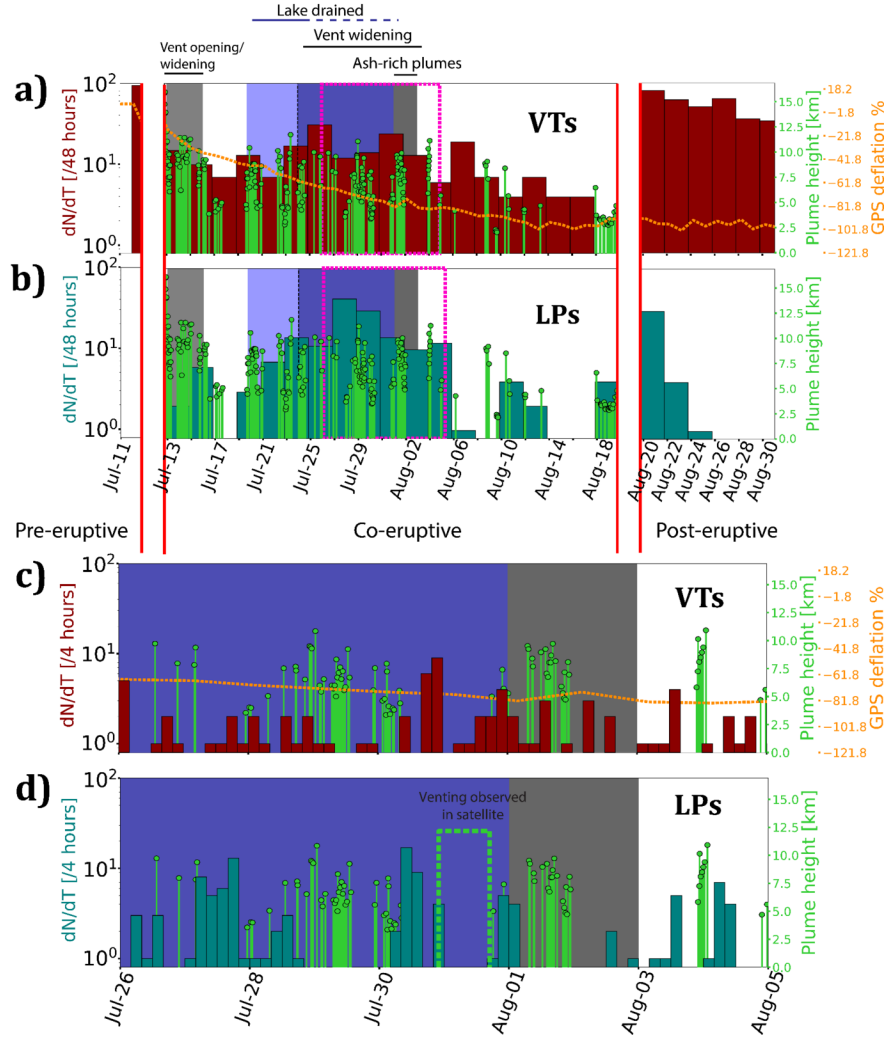


Figure 4. Seismicity rate over time . Number of earthquakes every 48 hrs for the eruptive sequence separated into pre-, co- and post-eruptive phases for VTs (a) and LPs (b), and a higher resolution (earthquakes/4 hrs) rate for VTs (c) and LPs (d) for the middle of the eruption (magenta frame in a,b). Note that the seismicity rate for the 3 eruptive phases in a) and b) has a different completeness level (see Figures 2, S6 and S7) and thus trends should only be interpreted within each time interval. VT earthquake rates and LP earthquake rate are shown in red and turquoise, respectively. GPS deflation percentage is shown with the dashed orange dashed line and the plume height observations (Larsen et al. 2009) are shown in green. Dashed green box shows time with otherwise unreported satellite observations of plumes (see text). Shaded areas correspond to the eruption chronology as shown by the horizontal lines above panel a).

The 48-hour seismicity rate (Figure 4a,b) reveals an interesting first order observation for the co-eruptive stage: the LPs occur only during times of plume activity, whereas the VTs are independent of the plume observations.

The first burst of LPs is observed after the initial phase of opening and widening of the main vents (July 13-16). After this, the LP rate shows a swarm-like pattern (e.g. Mogi, 1963; Benoit and McNutt, 1996; Zobin, 2012) with a large increase in rate of almost two orders of magnitude starting around July 20, following a cluster of plume observations. The swarm-like pattern peaks around the middle of the eruption (July 27) and

then quickly decreases toward August 8. The end of the eruption (~August 8-18) is marked by a substantial reduction of the LP rate, but immediately after the last plume emission (August 19), when the eruption officially ended and the volcano remained as a closed system, there was a large burst of post-eruptive LPs that decayed rapidly.

The peak of the swarm pattern (July 27) is the most significant co-eruptive seismic sequence. This period matches the widening of North Lake vent observed in SAR images (Larsen et al. 2015) and an increase of ash-rich plumes. Importantly, the short-period (4-hour) rates show that the LP bursts are not coincident in time with observations of large plumes from satellite images or written reports from AVO (Figure 4d). The discrepancy between increased LP rates and plume observations does not correspond to changes in noise or to missing data (Figure S9).

The behavior of the LP events can be contrasted with the VT events. A distinct population of VT earthquakes maintain a steadier seismicity rate during the eruption compared to the LPs. The VTs are also more distributed over a large region (Figures 2b,c) and do not decrease (or increase) in the period that the GPS shows as changing deflation rate (Figures 4a,c). Apart from the initial opening sequence, which we will address separately below, the VTs show a relatively stable rate until the onset of the widening of the North vent reported by Larsen et al. (2015) (July 24 to August 3), when the rate increases by a factor of two. The higher resolution 4-hour earthquake rate (Figures 4c,d) reveals that during the time when LPs do not coincide with periods of prominent plume observations the VTs show a steadier rate, except for a few small bursts that also do not coincide in time with the plumes. The VT rate has slight variations during the rest of the eruption but overall gradually decreases until the cessation of activity. The post-eruptive rate for the VTs shows a large jump of about an order of magnitude compared to the co-eruptive rate, and decays gradually, once again differentiating from the LPs rate behavior. Overall, the VTs rate is steadier than the LPs rate throughout the co-eruptive and post-eruptive phases of the eruption, and it does not correlate or anti-correlate with other geophysical observations.

Cycles of LPs and plumes

The difference in the overall behavior of the seismicity rate between VTs and LPs (i.e., relatively stable versus significantly variant), along with the LPs relation with plume activity, hints at different controlling mechanisms for the two types of signals throughout the eruption. To further investigate this, we inspect the middle stage of the eruption in more detail, when the rate of the long-period seismicity is at a cusp and Larsen et al. (2015) report the widening of the vents and a richer content of ash in the plumes. It is worth noting again that most of the VTs are more distributed in the caldera, with certain bursts around Cone A, while the majority of the LP earthquakes are highly clustered in the vicinity of the active vents and near the east side of the caldera rim (Figures 2b,c).

The middle sequence of the eruption probably initiated with the drainage of North Lake on July 19 and an ensuing escalation in continuous tremor (Larsen et al., 2015). This stage is marked by the largest number and magnitude of LP events. Throughout this period, bursts of LPs migrated from directly underneath Ahmanilix at 2-5 km depths (July 27), then progressed either to the southeast toward Cone D or to the east toward North Lake and clustered at shallower (~1 km) depths (July 30), and finally migrated east and south toward the caldera wall and Mount Tulik from July 31-August 1. Figure 5a shows the time series of the magnitudes of the LP events color coded by time since July 27, and Figures 5b-e show the relocations of the earthquakes hypocenters, where the migration from Ahmanilix to the caldera wall can be observed. Similar to Figure 4, the bursts of migrating LPs do not coincide in time with plume observations. This is even more evident when compared to the envelope of the time series (black curve on Figure 5a), where the peaks correspond to the bursty character of the LPs sequence and the troughs are matched by an increase in plume observations. There were at least three cycles of LP bursts during the middle of the eruption. The striking correspondence of the magnitudes envelope troughs to plumes even warned of a lack of plume observations during July 31, as

mentioned above. After a manual inspection of the available AVHRR images (Figure S8) we could confirm that, indeed, emissions were present at those times.

Interestingly, a second escalation in steady tremor on August 2, after the bursts of migrating LP events, migrated from North Lake to the caldera wall over a period of 1-2 hours (Haney, 2014) and was accompanied by a transient inflation signal in the GPS.

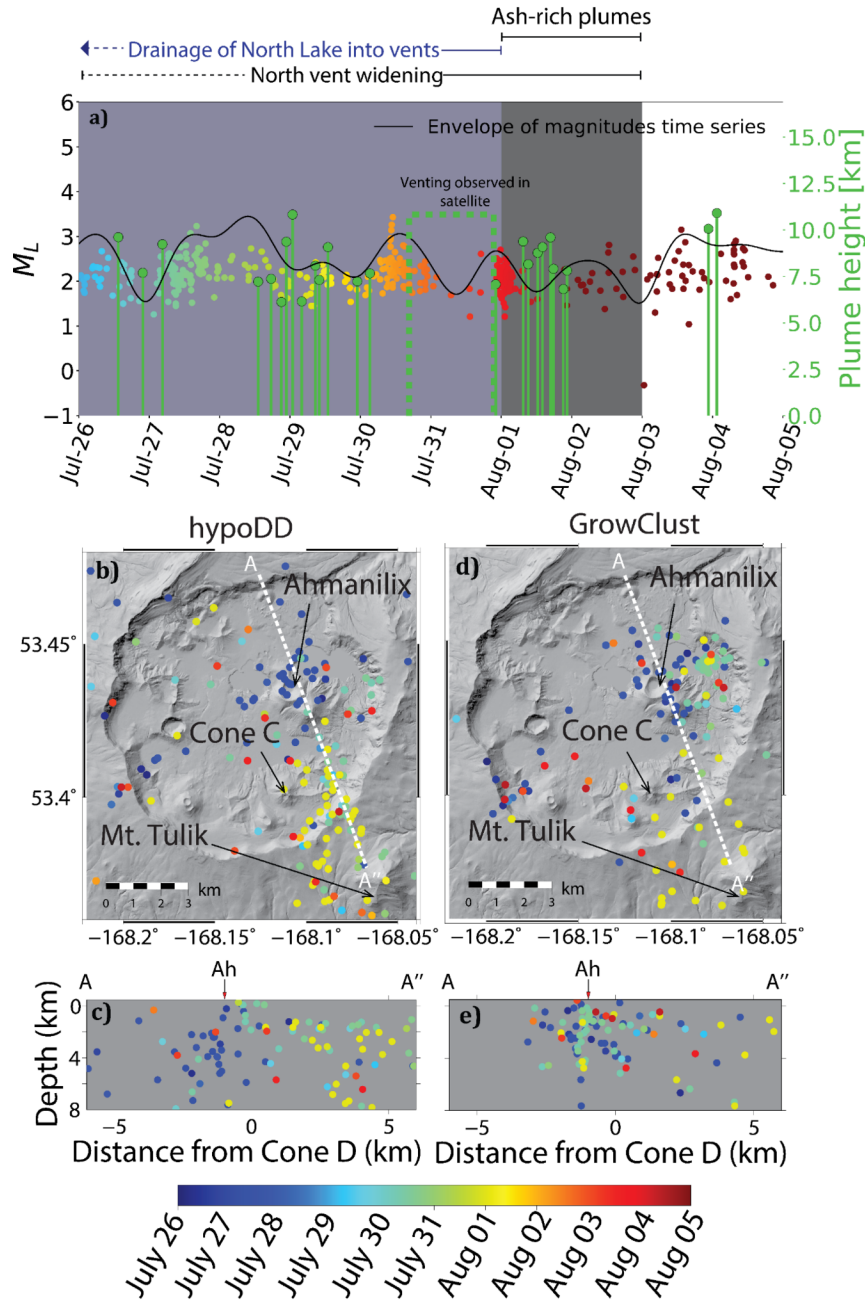


Figure 5. Migration of LP bursts during the middle of the eruption and lack of correspondence with plumes. a) Magnitudes over time for the LP bursts during the middle of the eruption. The black curve shows the envelope of the magnitudes envelope. Plume height observations are shown in green stems. b) Map

and c) cross-sectional view of the LP earthquakes (*hypoDD* relocations) during the most prominent bursts from July 27 to August 1, showing the migration pattern. All LPs are colored by days since July 27. d) and e) are *GrowClust* relocations. Note the criteria of the *GrowClust* algorithm results in fewer located events. Width of cross-section = 3 km; azimuth = 160°. Arrows: Ah=Ahmanilix.

Observation 2: Opening sequence

A major exception to the LP and VT behavior discussed above is the initial opening sequence of the eruption. The overall rate of the VT events (Figure 4a) is characterized by a single sharp burst (interpreted as run-up seismicity leading to the eruption), followed by a rate decrease of about one order of magnitude.

The opening sequence is entirely composed of VT earthquakes, and it extends to at least 14 km depth. The magnitudes during this runup period show a gradual increase leading to the onset of the eruption (Figure 6a). The seismicity is randomly distributed about the injection dyke (Figure 6b,c) and its end is marked by a migration over several minutes from Ahmanilix (i.e., the eruptive vent) toward the center of deformation the west (Figures 1 and 6d,e). This observation contrasts what has been observed in other large basaltic volcanoes, where the migration of earthquakes before the onset of the eruption is toward the eruptive site (Caudron et al., 2015; Duputel, 2019; Lengliné et al., 2021).

The earthquakes of the opening sequence are well-located underneath the ultimate eruptive vents at ~4-7 km depths. There is only a small cluster of shallow earthquakes underneath the maars craters that could be an indication of more vigorous hydro-magmatic interactions prior to the initial explosions. Earthquakes are absent at shallower depths under the vents during this period.

Ohlendorf et al. (2014) describe the earthquakes hypocenters of the opening sequence as a shallow (<6 km) planar feature striking WSW-NNE and dipping to the NNW. Our enhanced catalog illuminates an elongated structure striking W-E and dipping to the SE down to a depth of ~15 km (Figure 3a, Figure 6b-d). The earthquakes that are observed up to three hours before the eruption span the whole dipping structure and they have a small magnitude; however, during the last hour preceding the start of the eruption the earthquakes started concentrating at shallower depths (3-6 km). These results confirm the observations by Ohlendorf et al. (2014) on the progression of the earthquakes during the last minutes before the eruption, although the direction of the dip of the planar feature that they report differs from our results.

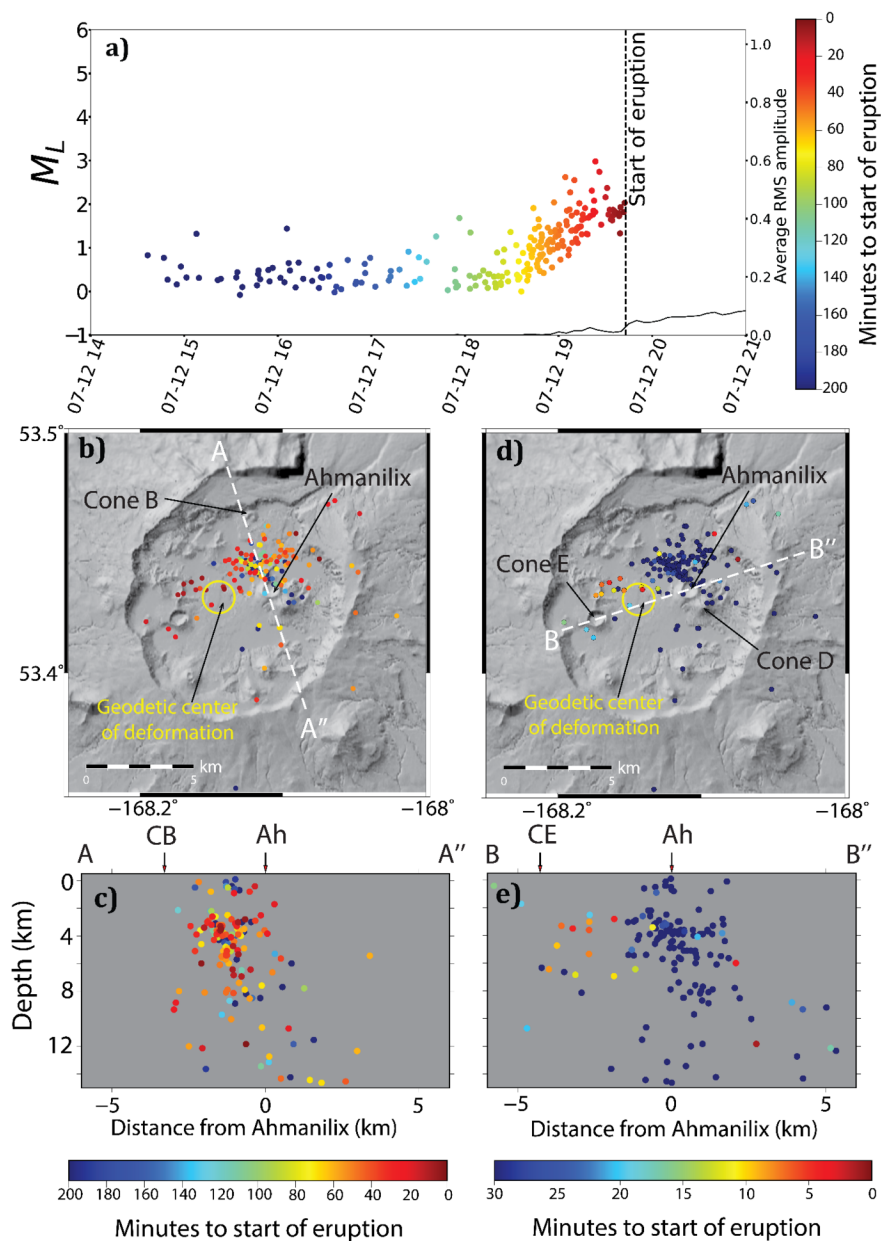


Figure 6. Timing (a) and location (b-e) of the VT sequence before the start of the eruption on July 12 19:43 UTC. Panels a-c have a color scale saturated at 200 minutes and panel d-e color scale saturates at 30 minutes before the eruption to show the migration of earthquakes toward the 2008 deflation source (yellow circle; Lu and Dzurisin, 2010) minutes before the start of the eruption. The azimuth of the cross-sections in c) and e) are 342° and 252° , respectively. Width of cross-sections = 5 km. Arrows: Ah=Ahmanilix; CE=Cone E; CB=Cone B.

Observation 3: The closing sequence of LP and VT earthquakes

The cessation of eruptive activity is marked by a sudden burst of LP earthquakes, which decayed rapidly with time, and was accompanied and followed by a steady stream of small VT earthquakes that occur south (and therefore distinct) from the previous concentration of seismicity. Shortly after the last plume of the eruption, the average RSAM reduced and there was a major increase in the number of small earthquakes observed in the southern sector of the caldera and also in distributed seismicity all over the southern part of the greater Okmok Volcano, all the way south to the isthmus of Umnak Island (Inanudak Bay, Figure 1). The post-eruptive seismicity involves a burst of LPs that started immediately after the last plume emission, and decayed rapidly with time, besides a high production of VT earthquakes that decayed slowly with time (Figures 4a,b). This post-eruptive population represents almost 40% of all the earthquakes detected from June 1 - August 31.

Surprisingly, there are very few earthquakes close to Ahamnilix or the other vents; rather, they are almost completely localized at the center of the caldera and under Cone A at ~4 km depth (Figure 3c), which is the depth of the estimated magma reservoir.

The end of the eruption also showed a change in geodetic behavior. Freymueller and Kaufman (2010) discuss the changes in the GPS deflationary trend that started 2-3 weeks after the main ash emissions based on a change in rate in the two GPS stations outside the caldera (OKSO and OKFG). Deflation was still ongoing until at least late September on OKFG, but an inflationary signal inside the caldera was recorded by station OKCE within 3 weeks of the end of the eruption. (There is an ambiguity on the exact timing due to a data gap.) They interpreted this as the result of deflation in a deep source and the immediate inflation of a shallow source.

Observation 4: volcano-tectonic b -value changes

The notion that b -values have a stress dependence and that tracking b -values over space and time can illuminate changes in the stress field is a common tenet in seismology (Scholz, 1968; 2015); variations in b -values have also been broadly explored in volcanoes (e.g., Bridges and Gao, 2006; Wyss et al., 2001; Garza-Giron, 2014) and low b -values are commonly interpreted as indicating high deviatoric stress. Since these theoretical principles apply to the accumulation of stress on rocks and their eventual failure, we focus our b -value analysis on volcano-tectonic events, which by definition represent the brittle failure of rocks (e.g., Roman, 2005). According to the above thinking, the b -values of the VT earthquakes must indicate the response of the host rocks of the volcano to the stress induced by the injection and extraction that undoubtedly took place before, during and after the eruption.

Figure 7 shows time variations of the b^+ estimator of the b -value, which is calculated as discussed in Sect 2.3, for the opening, co-eruptive and closing stages. The uncertainties shown in Figure 7 were calculated by 300 bootstrap realizations. All the 1-P values (P being the probability that two b values come from the same population; equation 1) for all the combinations of pairs of b^+ and b -values for the co-eruptive phase compared to before or after the eruption are lower than the 99% confidence limit, so we conclude that our results are highly statistically significant (Tables TS1 and TS2). The co-eruptive VTs have a larger b^+ than before or after the eruption. Even though the magnitudes of the earthquakes observed during the eruption are the highest, their distribution seems to favor smaller earthquakes, giving a relatively high b^+ (1.39 ± 0.07). Earthquakes in the opening and post-eruptive stages have a lower b^+ (1.13 ± 0.1 and 1.11 ± 0.05 , respectively), thus, the b -value would indicate that the stress concentration was higher during the pre- and post-eruptive periods. We also calculated the temporal variations of the b -value using a maximum-likelihood estimation (Utsu, 1965; Aki, 1965) and a least-squares computation. Even though they perform poorly compared to b^+ , we could confirm that the main observations are robust and independent of the estimator (Figures S5-S7).

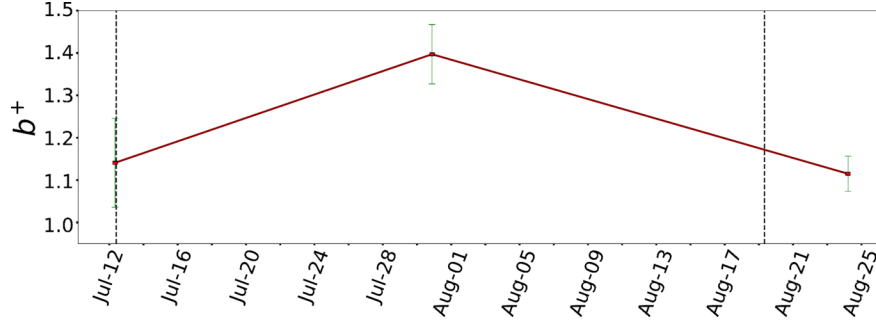


Figure 7. Values of b^+ before, during and after the eruption for VT earthquakes. The pre- and post-eruptive periods show a lower b^+ , suggesting higher stress levels. The error bars are based on 300 bootstraps.

All the b^+ (and b -values) computed for the three eruptive stages are anomalously high compared to b -values found in tectonically driven environments; however, this is very common for volcanic regions (McNutt, 1996; Wyss et al., 1997; Wyss et al., 2001; Roberts et al., 2015).

Observation 5: The enhanced eruption catalog reveals structural features of the volcano

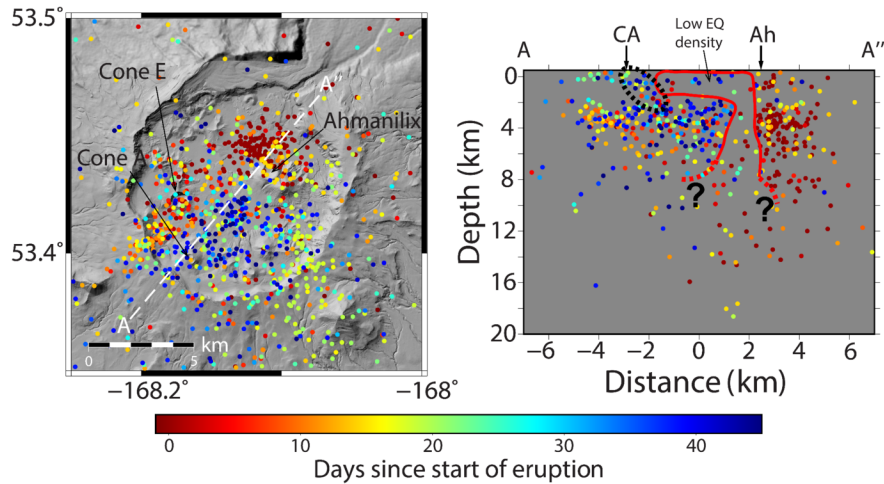


Figure 8. Relocated earthquake hypocenters using *hypoDD* for both VTs and LPs (colored by time since the eruption). The red-solid line indicates the volume of low earthquake density, coinciding with the initial source of deformation location from Lu and Dzurisin (2010), which progressed to depth over the course of the eruption. The dashed black ellipse indicates the only visible link of earthquakes that connect the 3-5 km deep cluster with Cone A. Width of cross-section = 2 km; azimuth = 40° . Arrows: CA=Cone A; Ah=Ahmanilix.

The relocated enhanced seismic catalog during the eruption has a comparable number of events to the catalog from 2001 to 2018. This allows for the study of the anatomy of the Okmok Volcano caldera and to illuminate the structures that were activated during the 2008 eruption. Figure 8 shows a map view and a cross section across the caldera with all events, VTs and LPs, color coded by time relative to the onset of the eruption.

The start of the eruption (red colors in Figure 8) is marked by earthquakes highly clustered under the active vents forming an elongated dipping structure as discussed in the opening sequence above (section 3.2). During the eruption, the VT earthquakes close to Cone A are the only visible link between the deep (~ 5 km) earthquakes and the shallow seismicity (observed in Figure 2c and marked with a black dashed ellipse in 8b). We note in passing an intriguing feature that is present in both relocated catalogs. There is an inverted boot-shaped volume that has low earthquake density (red outline in Figure 8; See also Figures S1 and S2) that surrounds the 2008 eruption vents and roughly coincides with the deformation foci inferred by GPS and InSAR analysis (Lu and Dzurisin, 2010; Xue et al., 2020). The quiescence suggests a region unable to accommodate elastic stresses large enough to trigger detectable earthquakes perhaps due to either the heat of the shallow magma system weakening the rocks or unconsolidated caldera fill. This earthquake-poor region is robust to location procedures as shown in Figures S1-S4. Alternatively, the lack of shallow seismicity could also be explained by low stress levels near the surface only allowing the rupture of very small earthquakes which are challenging to detect even with advanced detection methods (e.g., Duputel et al., 2019) or by trains of VT earthquakes being recorded as tremor and not detected as individual earthquakes (e.g. Eibl et al., 2017).

Summary of observations

A recapitulation of the clustering and migrations described above is reinforced by the more formal analysis of Figure 9. We follow the procedure of Sect. 2.2 to compute a correlation matrix for VT and LP events, where we can identify clusters of earthquakes in time. For each of the main clusters, we also calculated an epicentral centroid by using the median latitude and median longitude. The high noise level of the site results in a modal cross-correlation value of ~ 0.4 . Figure 9 emphasizes clusters that are much more correlated than this usual state by using a color scale that is saturated at three standard deviations from the mean values. Please refer to the supporting information (Figure S10) to see the cross-correlation matrix without a saturated scale.

The short-term runup of seismicity leading to the eruption (July 12) shows a cluster of well-correlated VT earthquakes from 14:00-18:00 UTC and a secondary group of earthquakes between 18:00-19:00 UTC. The centroid location of these two clusters suggests that the focus of pre-eruptive activity shifted from directly beneath the North Vent and Ahmanilix to the southwest toward the deflation source within minutes to the onset of the eruption. These observations confirm the pre-eruptive chronology described in the opening sequence (section 3.2) and it also matches the description by Ohlendorf et al. (2014), which noted the existence of these earthquake families. Thus, the correlation matrix quantitatively supports the visual identification of patterns discussed above.

The 48-hour rate of the LPs during the eruption showed that they are related to venting processes (Figure 4b), and the 4-hour rate, along with the envelope of the magnitudes time series, showed that the timing of the LPs bursts is not coincident with the timing of the plumes. The highest degree of clustering observed for the co-eruptive stage corresponds to bursts of LPs (outline boxes in Figure 9 right hand panel), and their centroids track the migration pattern described in section 3.1 (from Ahmanilix to the southeast caldera wall and Mount Tulik). The co-eruptive VT earthquakes show a more stable rate than the LPs and they do not track the deflation rate observed in GPS (Figure 4a). The VTs have a lower degree clustering for the co-eruptive earthquakes and the few well correlated VT events during this stage are clustered in the vicinity of Cone A.

The post-eruptive earthquakes occurred immediately after the last plumes observations, and they consist of a large burst of LP events that decayed rapidly in time (Figure 4b) and another large burst of VT events that decayed slowly in time (Figure 4a). These earthquakes in these post-eruptive bursts had lower magnitudes than those during the eruption. The clustering of these earthquakes is also visible in Figures 8 and 9. The centroids of the clusters are located near Cone A, and they occur mostly between 2 km and 4 km depths (Figure 8). Note that these clusters correspond to significant events in the eruption chronology, however,

the majority of events are not in the outlined clusters in Figure 9. The differences in cluster centroids from the hypoDD and GrowClust relocations show slight variations but are not significant for our interpretation (Figure S11).

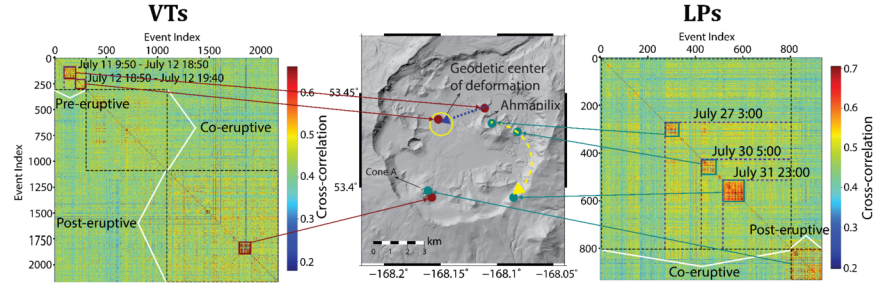


Figure 9. Cross-correlation matrix showing clustering. Events are sorted chronologically so low event indices correspond to the starting sequence and high indices correspond to post-eruptive earthquakes. The arrows point at the centroid of each cluster for the hypoDD relocations. Turquoise squares/arrows show LP activity. Red squares/arrows show VT activity. The dashed orange arrow shows the suggested precursory VT migration path toward the deflation source (yellow circle). The dashed yellow arrow shows the suggested co-eruptive LP migration path. The events are sorted in time following the numerical order. The locations of the co-eruptive VTs are not shown because they are broadly distributed.

Discussion

The combined seismological observations of rates, spatio-temporal patterns, frequency classification, b - values, and clustering allow us to make a conceptual model of the 2008 eruption of Okmok Volcano (Figure 10) and interpret the mechanisms for the three main stages of the eruption: before, during and after.

The most striking and important observation here is the distinct behavior of the LP and VT events. Therefore, we will focus our analysis on the mechanisms that generate the LP and VT earthquakes and how these are related to eruption dynamics. As we will discuss, the LPs appear to be an indication of fluid flow and can track dynamic changes in clogging and cracking during the eruption, whereas the VTs respond to the deviatoric stresses in the host rocks as injection and extraction occur during the three main stages of the eruption (before, during and after). This is in good agreement with the perception that long period earthquakes are related to fluid flow and high frequency VTs are generated due to failure on faults (Benson et al, 2008; Foulger et al., 2004; Roman, 2005).

LPs mechanism: clog and crack

Long-period earthquakes in volcanic systems have been attributed to effects such as resonance in fluid-filled cracks (Chouet 1996; Kumagai and Chouet, 1999; Haney et al., 2021), brittle failure in melt (Goto, 1999; Neuberg et al., 2006), slow rupture in either heated material (Harrington and Brodsky, 2007) or in unconsolidated material (Bean et al, 2014) and magma degassing (Melnik et al., 2020). Migration and burstiness of long period earthquakes in volcanic systems have been previously reported for the preparatory stage of volcanic eruptions and associated with pore-pressure transients in a hydraulically connected plumbing system (e.g. Shapiro et al., 2017; Frank et al., 2018). For the 2008 eruption, no LPs (shallow or deep) preceded the eruption, they are only observed for the co- and post-eruptive stages, and to our knowledge this is the first report of migrating bursts of LPs that are not correlated in time with plumes during a long-lived explosive eruption.

The long-period seismicity that is observed underneath the active vents during the middle of the eruption are undoubtedly related to the eruptive process and the immense amount of water accumulated in the subsurface of this area Unema et al. (2016). The middle eruption sequence commenced with the drainage of North Lake, which probably interacted with the ascending magma causing increased fragmentation and elevating the explosivity (Gonnerman, 2015). Given the timing, location and migration of these low-frequency earthquakes, but more importantly their lack of association with plumes, our preferred model is a clog-and-crack mechanism: The open vents become partially clogged, potentially by their own collapse, which might be seen at the surface as widening, or by plugs of ash-rich magma, allowing for pressure to build up in the subsurface (Figure 10b). The clogging restricts the flow of incoming magma and volatiles to the atmosphere and increases the pore-pressure at the conduit, which forces the fluids into existing permeable cracks causing volumetric changes that translate into the solid medium as low-frequency seismic radiation (Chouet, 1988,1996). An increase in pressure could also stress the surrounding heated or unconsolidated material to produce slow ruptures by brittle failure (Harrington and Brodsky, 2007). In either case, at some point, the accumulating pressure in the partially clogged system overcomes the clogging stress and cracks/opens triggering explosions that are followed by high altitude, dark (ash-rich) plumes and an LP rate reduction (Figure 10c). The energetic release of mass lasts until most of that pressure has been exhausted, allowing the re-clogging and triggering of a new LP burst. Note that there are few LPs still observed during the time of the emissions, which could be related to volumetric changes as the extraction of fluids takes place (Benson et al., 2008).

The clog-and-crack scenario presented above bears a striking resemblance to the valve opening/closing mechanism by Farge et al. (2021). This mechanism was proposed to explain low-frequency seismicity in subduction zones as bursts of tremor migrate along channels that experience abrupt changes in permeability when they get clogged by particles (closed valve) and unclogged by flow-induced stresses (open valve). The model by Farge et al. (2021) shows the emergence of the bursty and migratory behavior of low-frequency earthquakes, which is exactly what we observe for the co-eruptive LPs at Okmok Volcano.

The climatic middle sequence culminated as LPs gave way to a migrating high amplitude tremor at the vents (Haney, 2014) and the last large, ash-rich plumes of the eruption. The volcano seemed to have lost most of its eruptive power during these cycles of LPs and plumes events, and the eruption began to abate until the last emission was observed on August 19.

The last burst of LP events, which occurred after the last plume emissions, likely indicates the filling of available cracks with magmatic fluids and gases as the system remained permanently clogged and the shallow reservoir started to refill again (Figure 10d). This observation is supported by the relocation depth of the post-eruptive earthquakes hypocenters (Figure 8), which coincides with the depths of the magma reservoir suggested by other authors.

The clog-and-crack model presented here differs from the more general discussions of the significance of open and closed vent systems. The term “open system” is often used for degassing behavior, and is used to highlight how degassing behavior can be distinct from magma discharge behavior (e.g., Edmonds et al., 2022). Here, we only constrain the existence or not of plumes and have no direct constraints on the degassing and its relationship to magmatic processes. Furthermore, open volcanic systems in the degassing sense have been associated with high LP rates (Roman et al., 2019), whereas our “unclogged” system has a low LP rate during magmatic discharge.

In principle, another possibility is that one mechanism creates the LPs directly underneath the vents and a different one creates those close to the caldera wall and other intra-caldera cones (A and C). The LPs underneath the vent could be signaling strain-induced changes in fragmentation as magma batches migrate toward the surface (Papale, 1999; Gonnerman, 2015), whereas the LPs close to the caldera wall could be the manifestation of slow slip in patches of the ring fault structure. Such complexity cannot be ruled out, but the binary classification scheme used here does not find any distinction between the waveforms of the caldera wall and intra-caldera populations and the more complicated explanation is not favored for the migrating bursts simply because of the relationship to the plume emissions.

VTs mechanism: brittle failure as stress gauges

Whether they are triggered by magmatic intrusions or not, volcano-tectonic earthquakes are the signature of brittle failure in the rocks that make a volcano and its surroundings. Physically, they are not different from earthquakes that occur in non-volcanic media, and even their ability to trigger aftershocks is the same as non-volcanic earthquakes (Garza-Giron et al., 2018). Thus, they must also obey elastic and friction laws that depend on stressing rate changes in the medium (Dieterich, 1994; Kanamori and Brodsky, 2004). It is well known that the stress increase induced by the emplacement of dykes can cause large changes in seismicity rate of VT earthquakes, which are commonly matched by observations of crustal deformation (Dieterich et al., 2000; Segall, 2013; Rivalta et al., 2015). Consequently, analysis of VT earthquakes has become instrumental in forecasting eruptions (Roman et al., 2006; Ruppert et al., 2011; White & McCausland, 2016). However, little is known about the behavior of VTs during the extraction that takes place while the volcano is erupting. The observations presented here, based on seismicity rates, spatio-temporal patterns and changes in b -values, provide insight into the response of the rocks before, during and after the eruption as the volcanic system experienced injection, extraction and re-injection.

The largest changes in seismicity rate for the VTs are before and after the eruption (Figure 4). The runup seismicity is a clear example of earthquakes induced by stress changes likely caused by the injection of the dyke that triggered the eruption, and VTs are known to display different spatio-temporal patterns depending on the triggering mechanism related to the magma migration, which can vary from one eruption to another (Roman and Cashman, 2006). The pre-eruptive earthquakes observed here do not show a clear upward trend (i.e., vertical migration), instead they were randomly distributed around the dyke (Figure 6b,c). Therefore, we infer that for this eruption VTs were not triggered at the tip of the propagating dyke, but rather the Coulomb stress changes, promoted by the intrusion, induced slip on pre-existing faults which have a broad distribution of orientations (Roman, 2005).

The clog-and-crack systematics are manifested in the LP rate. However, the VTs that we measured do offer additional insight into the opening and closing of the system over a longer timescale. If high b -values indicate low stresses as suggested in prior work (Scholz 1958, 2015), then the time variation of b^+ -values of VT events (Figure 7) indicates that the elastic stresses in the edifice and surrounding rock were lower during the eruption than before and after. Evidently, the pre-eruptive sequence was triggered by an intrusion, so the VT generation is an indication of the stress accumulated in the subsurface as a closed system (low b^+) became highly pressurized due to the injection of magma (Figure 10a). Following the first blasts, the volcano became an open system, and the rocks experienced a reduction in deviatoric stresses (high b^+) as the eruption extracted material (middle panel in Figure 10). An increase in b -values after the onset of the eruption has also been observed in other eruptions (e.g. Shakirova and Firstov, 2022), but other eruptions have shown an opposite pattern with lower b -values after the onset of the eruption (Ibáñez et al., 2012). During the co-eruptive stage, VTs showed a steadier rate than the LPs and they did not follow the GPS deflation rate, implying that reservoir deflation was not the main source of stress during the eruption. Finally, for the post-eruptive phase (Figure 10d), the steadily decaying cascade of VT earthquakes immediately after the last emission, which were initially accompanied by a prominent burst of LPs that decayed quickly, are indicative of a large change in the stressing regime and faults being able to accumulate and release elastic strain again. Since the GPS station OKCE located inside the caldera (Cone E) showed a re-inflation signal when it was fixed by AVO staff shortly after the eruption ended, we interpret this as the seismic signature of a closed system (low b^+) which was stressed by an immediate reservoir replenishment process (i.e. an intrusion drawn into low-pressure pockets without overcoming the final clogging stress).

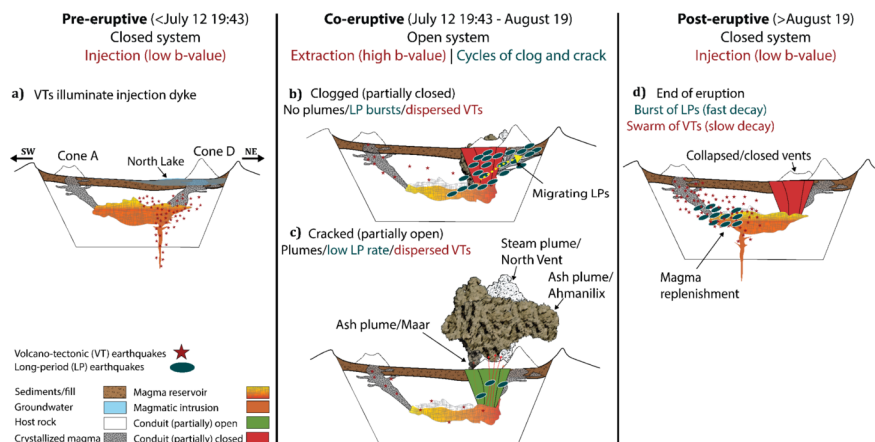


Figure 10. Cartoon of the evolution of the 2008 Okmok Volcano eruption. Left panel: a) Activation of a swarm of volcano-tectonic earthquakes induced by the injection of magma from a deep source into a ~ 4 km depth shallow reservoir. The orientation of the cross sectional view is SW-NE as indicated in panel a) and it is the same for all other panels. At this stage the volcano is a closed system and there is a high rate of stress change as shown by a low b -value of the VTs. The SW of the caldera at Okmok Volcano has a higher content of groundwater and surface lakes, which explains the phreato-magmatic nature of the eruption. North Lake is shown in panel a) due to its important role in the eruption. Center panel: After the eruption started following a large phreato-magmatic explosion, ash and steam plumes came out from at least four new major vents. During the extraction process the volcano is an open system and the stress and stressing rate are both lower than the initial phase (higher b -value of VTs). Toward the middle, North Lake drained into a vent and the eruption developed in cycles of clogging and cracking, potentially due to the collapse of the vents or changes in fragmentation. When the volcanic vents are clogged (b), long-period earthquake bursts migrate from the vents in the direction of the caldera wall. When the volcano overcomes the clogging stress and the vents are cracked open (c), there is mass transfer of fluids and ash into the atmosphere and very few earthquakes are observed. Right panel: d) The end of the eruption is marked by a burst of long-period earthquakes that is accompanied and followed by a large number of VT earthquakes, distributed in the south of the caldera. At this stage there was injection of magma into the shallow magma reservoir that increased the stress regime but that resulted in a failed intrusion. After this the volcano remained closed.

Conclusions

We analyzed an enhanced, relocated and frequency-classified (volcano-tectonic and long-period) earthquake catalog during an explosive volcanic eruption. The analysis shows that with such advanced data processing, we can illuminate the structure of the volcano with high resolution and gain information on fundamental dynamic interactions between the solid and fluid media during the eruption. The co-eruptive LP and VT events demonstrate distinct behavior, likely caused by and therefore diagnostic of different eruptive processes. LPs are strongly localized in space and time and directly precede or follow mass ejection, contrasting with the steady, widely distributed VTs.

Together, the seismicity defined how the eruption began, evolved, and ended, which is a major goal for volcanology (National Academies, 2017). The 2008 explosive eruption started with the injection of magma from a deep reservoir which triggered a swarm of VTs that were randomly distributed about the dyke. Minutes before the eruption, VTs migrated toward the geodetic center of deformation shown by other authors. The eruption then evolved through at least three opening and closing cycles that showed a distinctive pattern of seismicity that we term clog-and-crack. High seismicity rates half-way through the eruption disclose a series of migratory LP earthquakes that started with a burst directly beneath the eruptive vent, followed by

ash-rich plumes, and continued to the east and southeast with two other main bursts that were also followed by dark (ash-rich) plumes. The eruption also involved a distinct population of VT earthquakes that maintain a steadier rate over a large region of the caldera. These co-eruptive VTs have a higher b -value than before or after the eruption, suggesting that the extraction process induced lower levels of stress in the caldera than the pre- and post-eruptive injection. The end of the eruptive activity is marked by a sudden burst of LP earthquakes which are accompanied and followed by a steady stream of small VT earthquakes that occur south (and therefore distinct) from the previous concentration of seismicity. Given the association of LP events with the previous pressurization episodes, it is possible that the end of the eruption was marked by another intrusion that failed to reach the surface and thus sealed the system.

An overriding theme is the repeated closure with clogged vents, as signaled by the localized LPs and subsequent opening with eruptive plumes. Even the closure of the eruption appears to have been a variation of this cycle. The high-speed evolution of the vent and pressurization of the rock can be illuminated through these previously inaccessible observations and has provided new clarity into the stages of the 2008 Okmok Volcano eruption. In the future, advanced seismic processing pipelines may allow for a similar analysis which could help volcano observatories gain more insight into the eruptive dynamics in near real-time and allow decision makers during volcanic crises to benefit from seeing the eruptions clearly.

Acknowledgements

We are grateful to the staff of the Alaska Volcano Observatory for their heroic work in collecting the key data of this paper and their insightful feedback throughout this project. We also thank JGR Editor Rachel Abercrombie and Nikolai Shapiro, Philippe Lesage, Weston Thelen, David Shelly, and two anonymous reviewers for their helpful comments which improved this manuscript. This work was partially supported by a Mexican National Council for Science and Technology (CONACYT) Doctoral Scholarship to Garza-Giron and in part by NSF EAR-2102069. The DEM for Umnak Island was downloaded from the The Alaska Division of Geological and Geophysical Surveys (ADGGS) website (<https://elevation.alaska.gov>). We acknowledge the use of imagery from the NASA Worldview application (<https://worldview.earthdata.nasa.gov>) and NASA's Global Imagery Browse Services (GIBS), part of the NASA Earth Observing System Data and Information System (EOSDIS). The maps shown in this work were made using The Generic Mapping Tools (GMT) (Wessel et al., 2019). The majority of the seismological signal processing performed in this work was done using the Obspy Python package (Beyreuther et al., 2010). Any use of trade, firm or product names is for descriptive purposes only and does not imply endorsement by the U.S. Government.

Data and Materials

The catalogs used in this work are available at <https://zenodo.org/record/7682936>.

Supplementary references

- Aki, K. (1965). Maximum likelihood estimate of b in the formula $\log N = a - bM$ and its confidence limits. *Bull. Earthq. Res. Inst., Tokyo Univ.*, 43, 237-239.
- Larsen, J., Neal, C., Webley, P., Freymueller, J., Haney, M., McNutt, S., Schneider, D., Prejean, S., Schaefer, J. and Wessels, R. (2009). Eruption of Alaska volcano breaks historic pattern. *Eos, Transactions American Geophysical Union*, 90(20), 173-174.
- Lu, Z., and Dzurisin, D. (2010). Ground surface deformation patterns, magma supply, and magma storage at Okmok volcano, Alaska, from InSAR analysis: 2. Coeruptive deflation, July–August 2008. *Journal of Geophysical Research: Solid Earth*, 115(B5).

Trugman, D. T., and Shearer, P. M. (2017). GrowClust: A hierarchical clustering algorithm for relative earthquake relocation, with application to the Spanish Springs and Sheldon, Nevada, earthquake sequences. *Seismological Research Letters*, 88(2A), 379-391.

Utsu, T. (1965). A method for determining the value of "b" in a formula $\log n = a - bm$ showing the magnitude-frequency relation for earthquakes. *Geophys. Bull. Hokkaido Univ.*, 13, 99-103.

van der Elst, N. J. (2021). B-positive: A robust estimator of aftershock magnitude distribution in transiently incomplete catalogs. *Journal of Geophysical Research: Solid Earth*, 126(2), e2020JB021027.

Waldhauser, F., and Ellsworth, W. L. (2000). A double-difference earthquake location algorithm: Method and application to the northern Hayward fault, California. *Bulletin of the Seismological Society of America*, 90(6), 1353-1368.

Wiemer, S., and Wyss, M. (2000). Minimum magnitude of completeness in earthquake catalogs: Examples from Alaska, the western United States, and Japan. *Bulletin of the Seismological Society of America*, 90(4), 859-869.

References

Aki, K. (1965). Maximum likelihood estimate of b in the formula $\log N = a - bM$ and its confidence limits. *Bull. Earthq. Res. Inst., Tokyo Univ.*, 43, 237-239.

Albright, J. A., Gregg, P. M., Lu, Z., and Freymueller, J. T. (2019). Hindcasting magma reservoir stability preceding the 2008 eruption of Okmok, Alaska. *Geophysical Research Letters*, 46(15), 8801-8808.

Bean, C. J., De Barros, L., Lokmer, I., Métaxian, J. P., O'Brien, G., & Murphy, S. (2014). Long-period seismicity in the shallow volcanic edifice formed from slow-rupture earthquakes. *Nature geoscience*, 7 (1), 71-75.

Benoit, J. P., & McNutt, S. R. (1996). Global volcanic earthquake swarm database and preliminary analysis of volcanic earthquake swarm duration. *Annali di Geofisica*, 39(2), 221.

Benson, P. M., Vinciguerra, S., Meredith, P. G., & Young, R. P. (2008). Laboratory simulation of volcano seismicity. *Science*, 322 (5899), 249-252.

Beyreuther, M., Barsch, R., Krischer, L., Megies, T., Behr, Y., and Wassermann, J. (2010). ObsPy: A Python toolbox for seismology. *Seismological Research Letters*, 81 (3), 530-533.

Biggs, J., Lu, Z., Fournier, T., and Freymueller, J. T. (2010). Magma flux at Okmok Volcano, Alaska, from a joint inversion of continuous GPS, campaign GPS, and interferometric synthetic aperture radar. *Journal of Geophysical Research: Solid Earth*, 115(B12). <https://doi.org/10.1029/2010JB007577>.

Bridges, D. L., and Gao, S. S. (2006). Spatial variation of seismic 1alues beneath Makushin Volcano, Unalaska Island, Alaska. *Earth and Planetary Science Letters*, 245 (1-2), 408-415.

Buurman, H., West, M. E., and Power, J. A. (2006). Seismic precursors to volcanic explosions during the 2006 eruption of Augustine Volcano. *The*, 41-57.

Caudron, C., Taisne, B., Kugaenko, Y., and Saltykov, V. (2015). Magma migration at the onset of the 2012–13 Tolbachik eruption revealed by Seismic Amplitude Ratio Analysis. *Journal of Volcanology and Geothermal Research*, 307, 60-67.

Chouet, B. (1988). Resonance of a fluid-driven crack: Radiation properties and implications for the source of long-period events and harmonic tremor. *Journal of Geophysical Research: Solid Earth*, 93(B5), 4375-4400.

Chouet, B. A. (1996). Long-period volcano seismicity: its source and use in eruption forecasting. *Nature*, 380(6572), 309-316.

- Coats, R. R. (1950). Volcanic activity in the Aleutian Arc (pp. 35-49). US Government Printing Office.
- D'Auria, L., Koulakov, I., Prudencio, J., Cabrera-Perez, I., Ibanez, J.M., Barrancos, J., Garcia-Hernandez, R., Martinez van Dorth, D., Padilla, G.D., Przeor, M. and Ortega, V. (2022). Rapid magma ascent beneath La Palma revealed by seismic tomography. *Scientific Reports* , 12 (1), 17654.
- Dieterich, J. (1994). A constitutive law for rate of earthquake production and its application to earthquake clustering. *Journal of Geophysical Research: Solid Earth*, 99(B2), 2601-2618.
- Dieterich, J., Cayol, V., & Okubo, P. (2000). The use of earthquake rate changes as a stress meter at Kilauea volcano. *Nature*, 408(6811), 457-460.
- Duputel, Z., Lengline, O., and Ferrazzini, V. (2019). Constraining spatiotemporal characteristics of magma migration at Piton de la Fournaise volcano from pre-eruptive seismicity. *Geophysical Research Letters* , 46 (1), 119-127.
- Eibl, E. P., Bean, C. J., Vogfjord, K. S., Ying, Y., Lokmer, I., Mollhoff, M., ... and Pálsson, F. (2017). Tremor-rich shallow dyke formation followed by silent magma flow at Bardarbunga in Iceland. *Nature Geoscience* , 10 (4), 299-304.
- Edmonds, Marie, E. J. Liu, and K. V. Cashman (2022). Open-vent volcanoes fuelled by depth-integrated magma degassing. *Bulletin of Volcanology* 84.3, 1-27.
- Farge, G., Jaupart, C., & Shapiro, N. M. (2021). Episodicity and migration of low frequency earthquakes modeled with fast fluid pressure transients in the permeable subduction interface. *Journal of Geophysical Research: Solid Earth* , 126 (9), e2021JB021894.
- Foulger, G. R., Julian, B. R., Hill, D. P., Pitt, A. M., Malin, P. E., & Shalev, E. (2004). Non-double-couple microearthquakes at Long Valley caldera, California, provide evidence for hydraulic fracturing. *Journal of Volcanology and Geothermal Research* , 132 (1), 45-71.
- Fournier, T., Freymueller, J., and Cervelli, P. (2009). Tracking magma volume recovery at Okmok volcano using GPS and an unscented Kalman filter. *Journal of Geophysical Research: Solid Earth*, 114(B2).<https://doi.org/10.1029/2008JB005837>.
- Frank, W. B., Shapiro, N. M., & Gusev, A. A. (2018). Progressive reactivation of the volcanic plumbing system beneath Tolbachik volcano (Kamchatka, Russia) revealed by long-period seismicity. *Earth and Planetary Science Letters* , 493 , 47-56.
- Freymueller, J. T., and Kaufman, A. M. (2010). Changes in the magma system during the 2008 eruption of Okmok volcano, Alaska, based on GPS measurements. *Journal of Geophysical Research: Solid Earth*, 115(B12).
- Garza-Giron, R. (2014) Spatial variation of the b value under Popocatepetl Volcano and its relation with the magma chamber. (428928) [Bachelor's dissertation, Universidad Nacional Autonoma de Mexico, Mexico]. Repositorio de Tesis DGBSDI:<https://repositorio.unam.mx/contenidos/428928>.
- Garza-Giron, R., Brodsky, E. E., & Prejean, S. G. (2018). Mainshock-aftershock clustering in volcanic regions. *Geophysical Research Letters*, 45(3), 1370-1378.
- Gerstenberger, M., Wiemer, S., and Giardini, D. (2001). A systematic test of the hypothesis that the b value varies with depth in California. *Geophysical Research Letters* , 28 (1), 57-60.
- Gonnermann, H. M. (2015). Magma fragmentation. *Annual Review of Earth and Planetary Sciences* , 43 , 431-458.
- Goto, A. (1999). A new model for volcanic earthquake at Unzen Volcano: Melt rupture model. *Geophysical Research Letters* , 26 (16), 2541-2544.

- Grey, D. M. (2003). Post-caldera eruptions at Okmok volcano, Umnak Island, Alaska, with emphasis on recent eruptions from Cone A (Doctoral dissertation).
- Haney, M. M. (2010). Location and mechanism of very long period tremor during the 2008 eruption of Okmok Volcano from interstation arrival times. *Journal of Geophysical Research: Solid Earth*, 115(B10).
- Haney, M. M. (2014). Backprojection of volcanic tremor. *Geophysical Research Letters*, 41(6), 1923-1928.
- Haney, M. M., Buurman, H., Holtkamp, S., and McNutt, S. R. (2021). Monochromatic Long-Period Seismicity Prior to the 2012 Earthquake Swarm at Little Sitkin Volcano, Alaska. *Frontiers in Earth Science*, 9, 513.
- Harrington, R. M., & Brodsky, E. E. (2007). Volcanic hybrid earthquakes that are brittle-failure events. *Geophysical Research Letters*, 34(6).
- Ibanez, J. M., De Angelis, S., Diaz-Moreno, A., Hernandez, P., Alguacil, G., Posadas, A., & Perez, N. (2012). Insights into the 2011–2012 submarine eruption off the coast of El Hierro (Canary Islands, Spain) from statistical analyses of earthquake activity. *Geophysical Journal International*, 191(2), 659-670.
- Johnson, J. H., Prejean, S., Savage, M. K., and Townend, J. (2010). Anisotropy, repeating earthquakes, and seismicity associated with the 2008 eruption of Okmok volcano, Alaska. *Journal of Geophysical Research: Solid Earth*, 115(B9).
- Kanamori, H., & Brodsky, E. E. (2004). The physics of earthquakes. *Reports on progress in physics*, 67(8), 1429.
- Kumagai, H., & Chouet, B. A. (1999). The complex frequencies of long-period seismic events as probes of fluid composition beneath volcanoes. *Geophysical Journal International*, 138(2), F7-F12.
- Larsen, J., Neal, C., Webley, P., Freymueller, J., Haney, M., McNutt, S., Schneider, D., Prejean, S., Schaefer, J. and Wessels, R. (2009). Eruption of Alaska volcano breaks historic pattern. *Eos, Transactions American Geophysical Union*, 90(20), 173-174.
- Larsen, J., Neal, C. A., Schaefer, J. R., Kaufman, M., and Lu, Z. (2015). The 2008 phreatomagmatic eruption of Okmok Volcano, Aleutian Islands, Alaska: chronology, deposits, and landform changes (No. RI 2015-2). Alaska Division of Geological and Geophysical Surveys.
- Lengline, O., Duputel, Z., and Okubo, P. G. (2021). Tracking dike propagation leading to the 2018 Kilauea eruption. *Earth and Planetary Science Letters*, 553, 116653.
- Lu, Z., T. Masterlark, and D. Dzurisin (2005), Interferometric synthetic aperture study of Okmok volcano, Alaska: Magma supply dynamics and post-emplacement lava flow deformation, *J. Geophys. Res.*, 110, B02403, doi:10.1029/2004JB003148.
- Lu, Z., and Dzurisin, D. (2010). Ground surface deformation patterns, magma supply, and magma storage at Okmok volcano, Alaska, from InSAR analysis: 2. Coeruptive deflation, July–August 2008. *Journal of Geophysical Research: Solid Earth*, 115(B5).
- Masterlark, T., Haney, M., Dickinson, H., Fournier, T., & Searcy, C. (2010). Rheologic and structural controls on the deformation of Okmok volcano, Alaska: FEMs, InSAR, and ambient noise tomography. *Journal of Geophysical Research: Solid Earth*, 115(B2).
- McNutt, S. R. (1996). Seismic monitoring and eruption forecasting of volcanoes: a review of the state-of-the-art and case histories. *Monitoring and mitigation of volcano hazards*, 99-146.
- Mann, D., Freymueller, J., & Lu, Z. (2002). Deformation associated with the 1997 eruption of Okmok volcano, Alaska. *Journal of Geophysical Research*, 107(B4), ETG 7-1–ETG 7-12. <https://doi.org/10.1029/2001JB000163>.

- Melnik, O., Lyakhovsky, V., Shapiro, N. M., Galina, N., & Bergal-Kuvikas, O. (2020). Deep long period volcanic earthquakes generated by degassing of volatile-rich basaltic magmas. *Nature communications* , 11 (1), 3918.
- Mogi, K. (1963). Some discussions on aftershocks, foreshocks and earthquake swarms: the fracture of a semi-infinite body caused by an inner stress origin and its relation to the earthquake phenomena (third paper). , 41 (3), 615-658.
- National Academies of Sciences, Engineering and Medicine. (2017). Volcanic eruptions and their repose, unrest, precursors, and timing. National Academies Press.
- Neuberg, J. W., Tuffen, H., Collier, L., Green, D., Powell, T., & Dingwell, D. (2006). The trigger mechanism of low-frequency earthquakes on Montserrat. *Journal of Volcanology and Geothermal Research*, 153(1-2), 37-50.
- Newhall, C. G., and Self, S. (1982). The volcanic explosivity index (VEI) an estimate of explosive magnitude for historical volcanism. *Journal of Geophysical Research: Oceans* , 87 (C2), 1231-1238.
- Ohlendorf, S. J., Thurber, C. H., Pesicek, J. D., and Prejean, S. G. (2014). Seismicity and seismic structure at Okmok Volcano, Alaska. *Journal of volcanology and geothermal research* , 278 , 103-119.
- Papale, P. (1999). Strain-induced magma fragmentation in explosive eruptions. *Nature* , 397 (6718), 425-428.
- Petersen, T. (2007). Swarms of repeating long-period earthquakes at Shishaldin Volcano, Alaska, 2001–2004. *Journal of Volcanology and Geothermal Research* , 166 (3-4), 177-192.
- Power, J. A., Friberg, P. A., Haney, M. M., Parker, T., Stihler, S. D., & Dixon, J. P. (2019). *A unified catalog of earthquake hypocenters and magnitudes at volcanoes in Alaska—1989 to 2018* (No. 2019-5037). US Geological Survey.
- Rivalta, E., Taisne, B., Bungler, A. P., & Katz, R. F. (2015). A review of mechanical models of dike propagation: Schools of thought, results and future directions. *Tectonophysics*, 638, 1-42.
- Roberts, N. S., Bell, A. F., and Main, I. G. (2015). Are volcanic seismic b-values high, and if so when?. *Journal of Volcanology and Geothermal Research* , 308 , 127-141.
- Roman, D. C. (2005). Numerical models of volcanotectonic earthquake triggering on non-ideally oriented faults. *Geophysical Research Letters* , 32 (2).
- Roman, D. C., & Cashman, K. V. (2006). The origin of volcano-tectonic earthquake swarms. *Geology*, 34(6), 457-460.
- Roman, D. C., Neuberg, J., & Luckett, R. R. (2006). Assessing the likelihood of volcanic eruption through analysis of volcanotectonic earthquake fault–plane solutions. *Earth and Planetary Science Letters*, 248(1-2), 244-252.
- Roman, D. C., LaFemina, P. C., Bussard, R., Stephens, K., Wauthier, C., Higgins, M., ... & Tenorio, V. (2019). Mechanisms of unrest and eruption at persistently restless volcanoes: Insights from the 2015 eruption of Telica Volcano, Nicaragua. *Geochemistry, Geophysics, Geosystems* , 20 (8), 4162-4183.
- Ruppert, N. A., Prejean, S., & Hansen, R. A. (2011). Seismic swarm associated with the 2008 eruption of Kasatochi Volcano, Alaska: Earthquake locations and source parameters. *Journal of Geophysical Research: Solid Earth*, 116(B2).
- Segall, P. (2013). Volcano deformation and eruption forecasting. Geological Society, London, Special Publications, 380(1), 85-106.
- Seropian, G., Kennedy, B. M., Walter, T. R., Ichihara, M., & Jolly, A. D. (2021). A review framework of how earthquakes trigger volcanic eruptions. *Nature Communications* , 12(1), 1-13

- Shakirova, A., and Firstov, P. (2022). Features of the Kizimen Volcano area seismicity prior to and during the 2010–2013 eruption. *Journal of Volcanology and Geothermal Research* , 421 , 107420.
- Shapiro, N. M., Droznin, D. V., Droznina, S. Y., Senyukov, S. L., Gusev, A. A., & Gordeev, E. I. (2017). Deep and shallow long-period volcanic seismicity linked by fluid-pressure transfer. *Nature Geoscience* ,10 (6), 442-445.
- Scholz, C. H. (1968). The frequency-magnitude relation of microfracturing in rock and its relation to earthquakes. *Bulletin of the seismological society of America* , 58 (1), 399-415.
- Scholz, C. H. (2015). On the stress dependence of the earthquake b value. *Geophysical Research Letters* , 42 (5), 1399-1402.
- Schorlemmer, D., Wiemer, S., and Wyss, M. (2005). Variations in earthquake-size distribution across different stress regimes. *Nature* , 437 (7058), 539-542.
- Thelen, W., Malone, S., and West, M. (2011). Multiplets: Their behavior and utility at dacitic and andesitic volcanic centers. *Journal of Geophysical Research: Solid Earth* , 116 (B8).
- Trugman, D. T., and Shearer, P. M. (2017). GrowClust: A hierarchical clustering algorithm for relative earthquake relocation, with application to the Spanish Springs and Sheldon, Nevada, earthquake sequences. *Seismological Research Letters*, 88(2A), 379-391.
- Umakoshi, K., Takamura, N., Shinzato, N., Uchida, K., Matsuwo, N., and Shimizu, H. (2008). Seismicity associated with the 1991–1995 dome growth at Unzen Volcano, Japan. *Journal of volcanology and geothermal research* , 175 (1-2), 91-99.
- Unema, J. A., Ort, M. H., Larsen, J. F., Neal, C. A., and Schaefer, J. R. (2016). Water-magma interaction and plume processes in the 2008 Okmok eruption, Alaska. *Bulletin*, 128(5-6), 792-806.
- Utsu, T. (1965). A method for determining the value of "b" in a formula $\log n = a - b m$ showing the magnitude-frequency relation for earthquakes. *Geophys. Bull. Hokkaido Univ.*, 13, 99-103.
- van der Elst, N. J. (2021). B-positive: A robust estimator of aftershock magnitude distribution in transiently incomplete catalogs. *Journal of Geophysical Research: Solid Earth*, 126(2), e2020JB021027.
- Vergnolle, S., & Métrich, N. (2021). Open-vent volcanoes: a preface to the special issue. *Bulletin of Volcanology* , 83 (5), 29.
- Waldhauser, F., and Ellsworth, W. L. (2000). A double-difference earthquake location algorithm: Method and application to the northern Hayward fault, California. *Bulletin of the Seismological Society of America*, 90(6), 1353-1368.
- Wang, J., Lu, Z., & Gregg, P. M. (2021). Inflation of Okmok volcano during 2008–2020 from PS analyses and source inversion with finite element models. *Journal of Geophysical Research: Solid Earth*, 126(10), e2021JB022420.
- Wessel, P., Luis, J. F., Uieda, L., Scharroo, R., Wobbe, F., Smith, W. H. F., and Tian, D. (2019). The generic mapping tools version 6. *Geochemistry, Geophysics, Geosystems* , 20 (11), 5556-5564.
- White, R., & McCausland, W. (2016). Volcano-tectonic earthquakes: A new tool for estimating intrusive volumes and forecasting eruptions. *Journal of Volcanology and Geothermal Research*, 309, 139-155.
- Wiemer, S., and Wyss, M. (2000). Minimum magnitude of completeness in earthquake catalogs: Examples from Alaska, the western United States, and Japan. *Bulletin of the Seismological Society of America*, 90(4), 859-869.
- Wyss, M., Shimazaki, K., and Wiemer, S. (1997). Mapping active magma chambers by b values beneath the off-Ito volcano, Japan. *Journal of Geophysical Research: Solid Earth* , 102 (B9), 20413-20422.

Wyss, M., Klein, F., Nagamine, K., and Wiemer, S. (2001). Anomalous high b-values in the South Flank of Kilauea volcano, Hawaii: evidence for the distribution of magma below Kilauea's East rift zone. *Journal of Volcanology and Geothermal Research* , 106 (1-2), 23-37.

Xue, X., Freymueller, J., and Lu, Z. (2020). Modeling the post-eruptive deformation at Okmok based on the GPS and InSAR time series: Changes in the shallow magma storage system. *Journal of Geophysical Research: Solid Earth* , 125 (2), e2019JB017801.

Zobin, V.M. (2012). Introduction to Volcanic Seismology, 2nd edition, Elsevier, ISBN9780444563750.

Supporting Information

S1. GrowClust relocations and differences with hypoDD

In this section we show the earthquake hypocenters relocated by GrowClust (Trugman and Shearer, 2017) and how they compare to the hypoDD (Waldhauser and Ellsworth, 2000) relocated hypocenters. The main goal of this section is to demonstrate that the interpretations made in this paper are robust and independent of the relocation algorithm. Figures S1 and S3 show the map and cross-sectional view of the GrowClust hypocenters for a close-up view of the caldera of Okmok Volcano and the overall region of Umnak Island, respectively. The events are color-coded by the time relative to the start of the eruption. Figures S2 and S4 display the same view as Figure S1 and S3 ,respectively, but with an overlay of the hypoDD and GrowClust hypocenters. As can be seen in the four figures, the relocations delineate the same structural features of the volcano. For example, it can be clearly seen from Figures S1 and S2 that the inverted boot-shape area with low earthquake density discussed in the main text (red curve), as well as the connection between the 3-6 km deep cluster and Cone A (black ellipse) are also present in the GrowClust catalog and visible even when overlaying the two relocations results. Similarly, Figures S3 and S4 confirm that both relocations delineate the magmatic intrusion that initiated the 2008 eruption (panel a in both figures). They also show the lack of shallow events during the eruption and that most co-eruptive earthquakes are contained in a bowl-shaped volume (panel b) as well as the clustering of earthquakes in the southern sector of the caldera at depths of 3-6 km during the post-eruptive period, which we interpret as the replenishment of the magma reservoir.

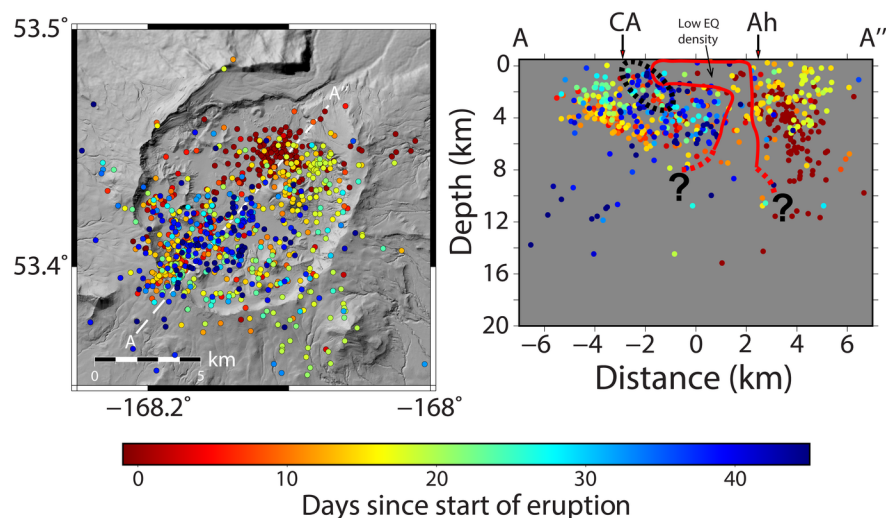


Figure S1. Relocated earthquake hypocenters using GrowClust (colored by time since the start of the eruption). Both VTs and LPs are included. The red line indicates the volume of low earthquake density, coinciding with the initial source of deformation location from Lu and Dzurisin (2010), which progressed to depth over the course of the eruption. The dashed black ellipse indicates the only visible link of earthquakes that connect the 3-5 km deep cluster with Cone A. Width of cross-section = 2 km; azimuth = 40° . Arrows: CA=Cone A; Ah=Ahmanilix.

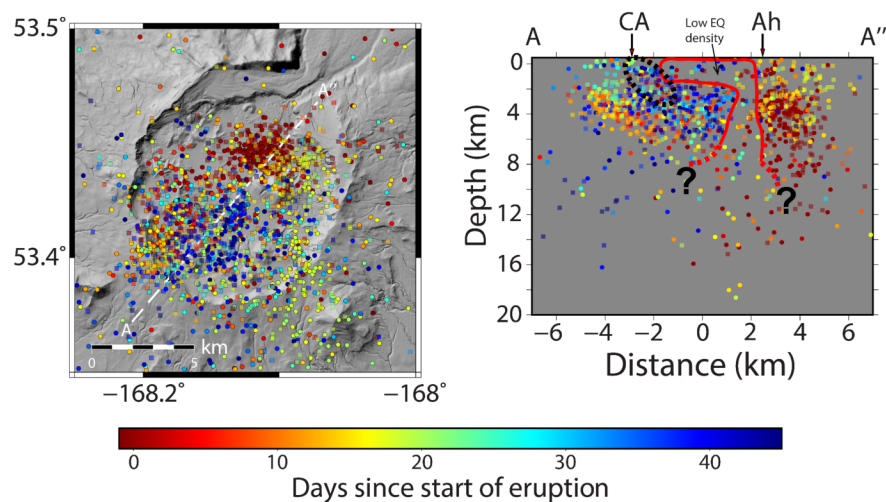


Figure S2. Overlay of the earthquake hypocenters using both hypoDD (solid circles) and GrowClust (faded squares). Both VTs and LPs are included. Events are color-coded relative to the time from the start of the eruption. Most of the features presented in the main text are clearly visible here, meaning that the two relocation algorithms illuminate the same structures during the eruptive period. The red-solid line indicates

the volume of low earthquake density, coinciding with the initial source of deformation location from Lu and Dzurisin (2010), which progressed to depth over the course of the eruption. The dashed black ellipse indicates the only visible link of earthquakes that connect the 3-5 km deep cluster with Cone A. Width of cross-section = 2 km; azimuth = 40°. Arrows: CA=Cone A; Ah=Ahmanilix.

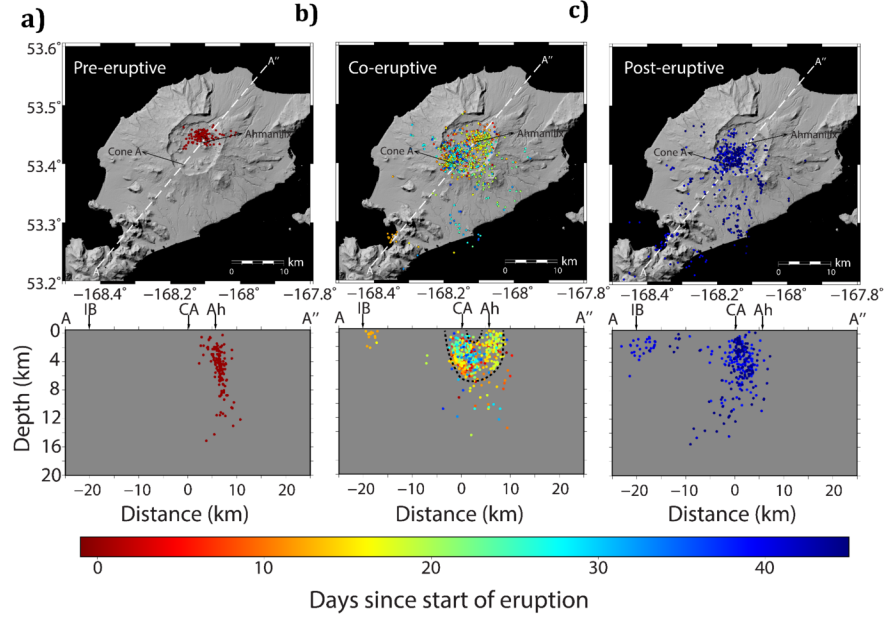


Figure S3. GrowClust relocated events before (a), during (b) and after (c) the eruption. The patterns seen in this figure are almost identical to the ones seen in the hypocenter relocations of hypoDD (Figure 3 in manuscript). The sequence leading up to the eruption clusters mainly underneath the vents that developed during the eruption; the co-eruptive seismicity shows a bowl-shaped volume (dashed line) inside the caldera with most of the activity occurring under Cone A and Ahmanilix; the post-eruptive sequence is governed by earthquakes in the south sector of the caldera most of them in the vicinity of Cone A. Cross sectional width = 3 km/azimuth = 40°. Arrows: Ah=Ahmanilix; CA=Cone A; IB=Inanudak Bay.

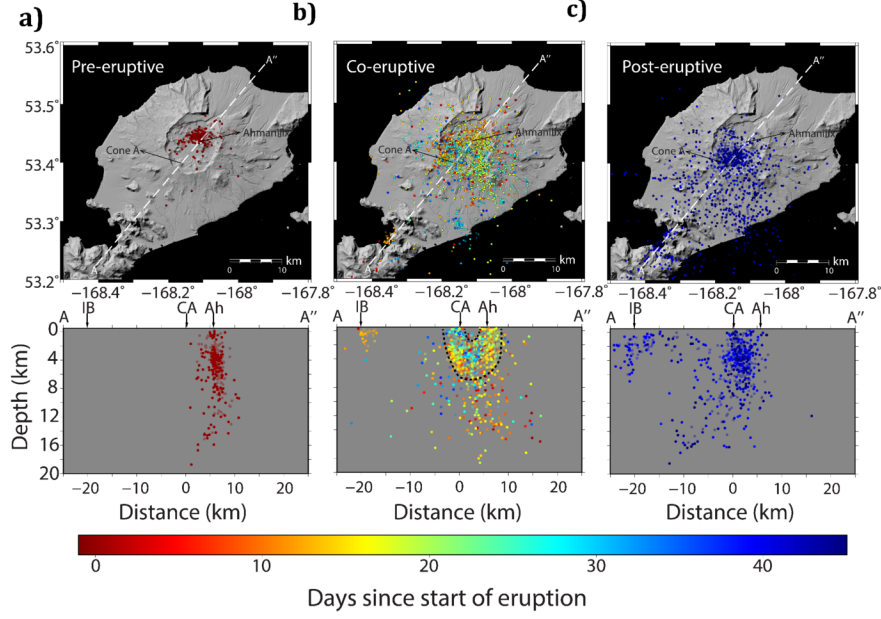


Figure S4. Overlay of hypoDD (solid) and GrowClust (transparent) hypocenter relocations before (a), during (b) and after (c) the eruption. The patterns seen in this figure are almost identical to the ones seen in the hypocenter relocations of hypoDD (Figure 3 in manuscript). This figure shows that the main features interpreted in the main text are robust to the relocation method. Cross sectional width = 3 km/azimuth = 40°. Arrows: Ah=Ahmanilik; CA=Cone A; IB=Inanudak Bay.

S2. b -positive (b^+) and b -values

In this section we present the tables and plots of the results of the frequency-magnitude distribution parameters calculated for volcano-tectonic events at different stages of the eruption (i.e. pre-eruptive, co-eruptive and post-eruptive) as well as the associated uncertainties and their statistical significance measured with the P values (see main text). Figure S5 shows the b^+ measurements, which correspond to the slope of the cumulative distribution function of the positive differences of consecutive magnitudes (van der Elst, 2021). Figures S6 and S7 show the b -value measured by the customary maximum-likelihood (Aki, 1965; Utsu, 1965) and least-squares methods, respectively.

For the co- and post-eruptive sequence, the completeness magnitude was determined by the maximum curvature method plus a correction of 0.1 to compensate for the common underestimation of M_c (Wiemer and Wyss, 2000). Magnitudes were rounded to two significant figures (i.e. $\Delta M = 0.01$). For the pre-eruptive sequence, multiple breaks in slope resulted in an unrealistically low magnitude of completeness using the automated method, therefore we adjusted the magnitude of completeness to a more conservative value of 1.4 based on the break in slope as seen in Figures S6 and S7.

The three methods used to estimate the b -value all indicate that the b -values during the eruption are higher than before or after.

S2.1. b^- -positive

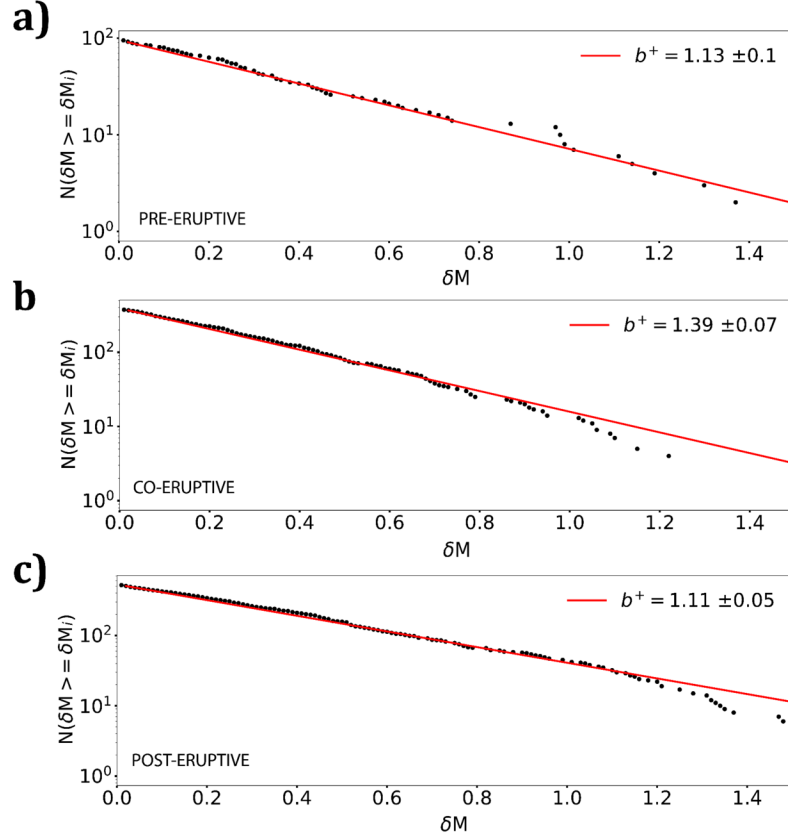


Figure S5. b^+ estimation (van der Elst, 2021) during the pre-eruptive (a), co-eruptive (b) and post-eruptive (c) phases of the eruption. The b^+ parameter is calculated from the slope of the cumulative distribution function of the positive differences of sequential magnitudes. The b^+ during the eruption is higher than before and after, suggesting that the deviatoric stresses for the co-eruptive phase were lower.

S2.2. Maximum-likelihood

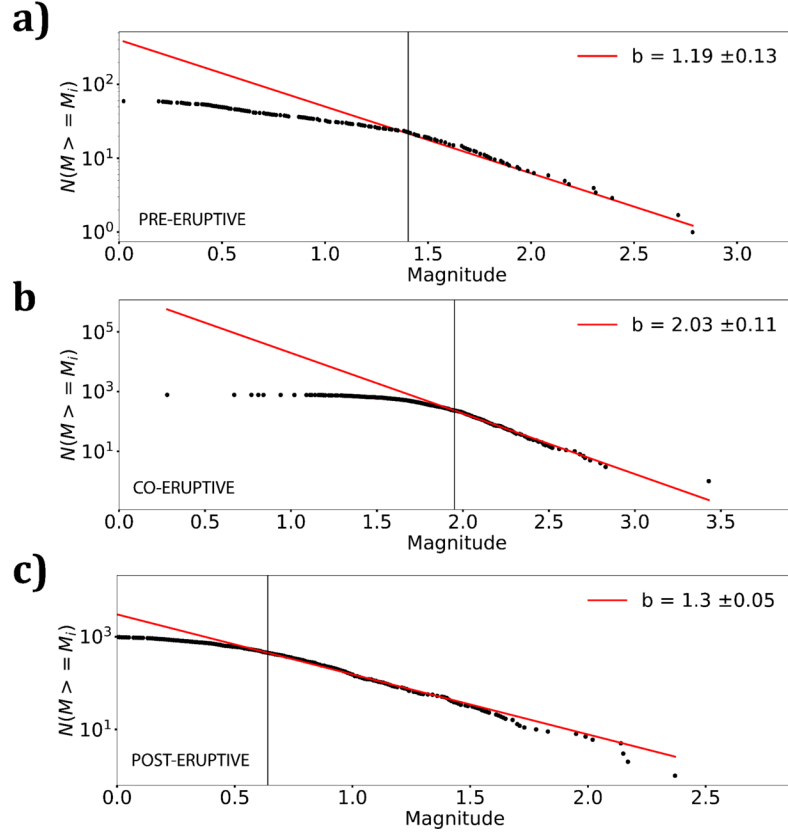


Figure S6. Maximum-likelihood estimate of the b -value (Aki, 1965; Utsu, 1965) during the pre-eruptive (a), co-eruptive (b) and post-eruptive (c) phases of the eruption. The magnitude of completeness of each sequence is as shown by the vertical lines as described in the accompanying text. Similar to the b^+ estimation, the highest b -value is observed during the eruption.

S.2.3 Least-squares

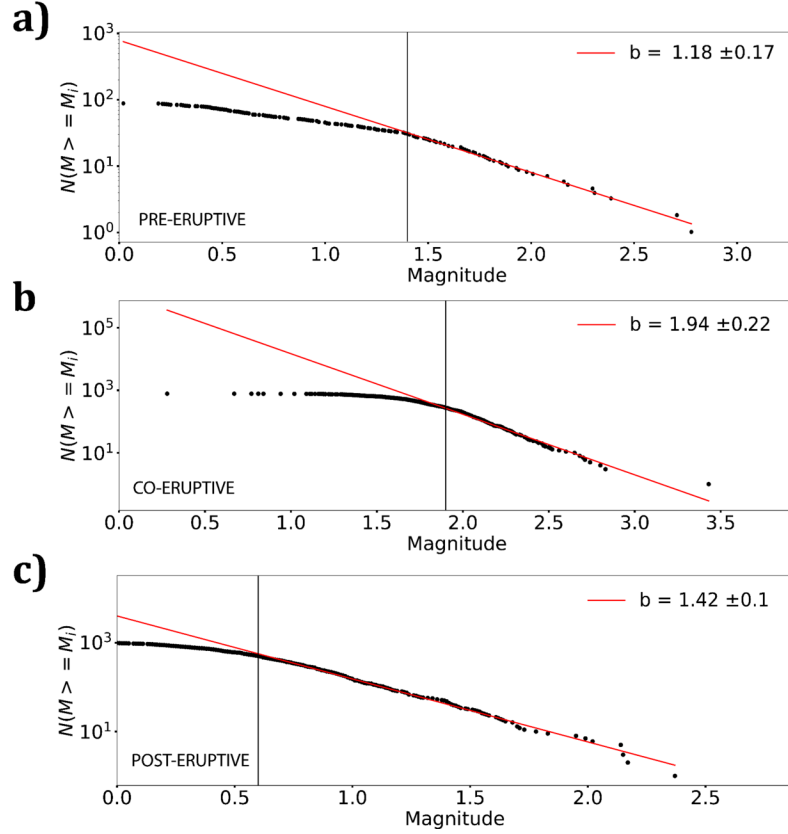


Figure S7. Least-squares estimate of the b -value during the pre-eruptive (a), co-eruptive (b) and post-eruptive (c) phases of the eruption. The magnitude of completeness of each sequence is as shown by the vertical lines as described in the accompanying text. The least-squares method also shows that the highest b -value is observed during the eruption, confirming the calculations made using the b^+ and maximum-likelihood estimations.

Period/Parameter	Mc	b_{ML}	b_{LS}	b^+
Start	0.83	1.19 ± 0.13	1.18 ± 0.17	1.13 ± 0.1
Eruption	1.95	2.03 ± 0.11	1.94 ± 0.22	1.39 ± 0.07
End	0.64	1.3 ± 0.05	1.42 ± 0.1	1.11 ± 0.05

Table S1. Frequency-magnitude distribution parameters for the different eruption stages using different estimators (before, during and after; maximum-likelihood, least-squares, b^+) using VT earthquakes only.

Periods/P value	$P_{b_{ML}} \mid 1-P_{b_{ML}}$	$P_{b_{LS}} \mid 1-P_{b_{LS}}$	$P_{b^+} \mid 1-P_{b^+}$
Start-Eruption	$3e-4 \mid >99.96\%$	$2e-4 \mid >99.98\%$	$5.9e-2 \mid 94.1\%$
Start-End	$3.6e-1 \mid >63.44\%$	$1.5e-1 \mid >84.12\%$	$3.6e-1 \mid 63.44\%$
Eruption-End	$1.7e-7 \mid >99.99\%$	$1.3e-6 \mid >99.99\%$	$1.7e-3 \mid 99.82\%$

Table S2. Utsu test, i.e. P values (see main text), for testing the significance of the comparison between

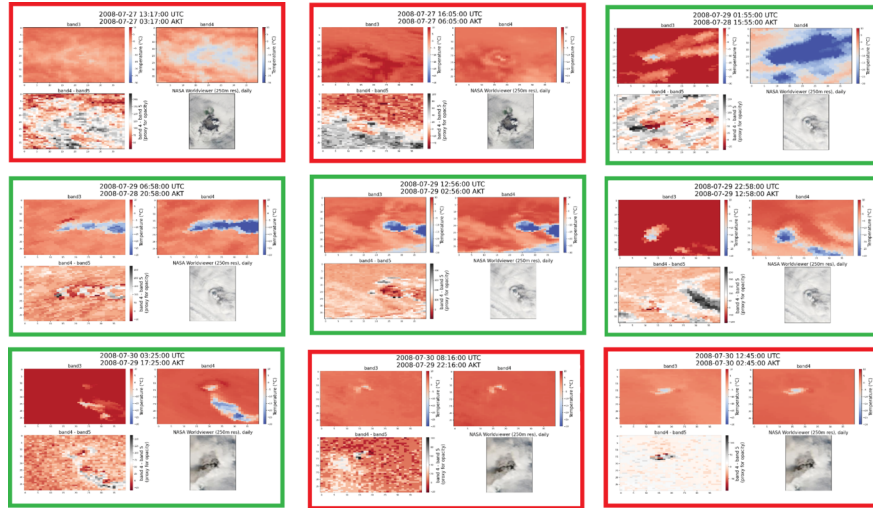
the parameters calculated in table S1.

S3. Plume data from satellite observations

Each green stem in Figures 4, 5 and S9 is a plume height measured from satellite data. Each data point is a recorded brightness-derived temperature based on the coldest point in the satellite data. The height at which the plume reaches thermal equilibrium with the surrounding atmosphere is inferred to be the plume height. While there are more advanced methods available today using data from new sensors that have been launched since 2008, this method is appropriate for the data available at the time of the Okmok eruption.

The Advanced Very High Resolution Radiometer (AVHRR) satellite imagery is only available when there is a satellite overpass, as it is polar orbiting. In 2008 there were four satellites with the AVHRR sensor onboard (NOAA-15 - NOAA-18). This led to an average of 0.98 satellite overpass per hour from 12 July - 19 August 2008, varying between 1.6 and 0.2/hr. This is based on examining the number of passes in 6 hour windows.

Figure S8 shows 23 different time frames of the AVHRR data using bands 3, 4 and 5 from July 27 to August 1, the period of time when we observe the migration of bursts of LP earthquakes and after which the eruption started abating. We analyzed these images to confirm the presence (green frames) or absence (red frames) of plumes during this key stage of the eruption. The images of July 29 clearly show the expected observation during the time of the ejection of a significant plume. On July 27 (during the LP bursts) the plume signal was so weak that one can even see the silhouette of Okmok Volcano.



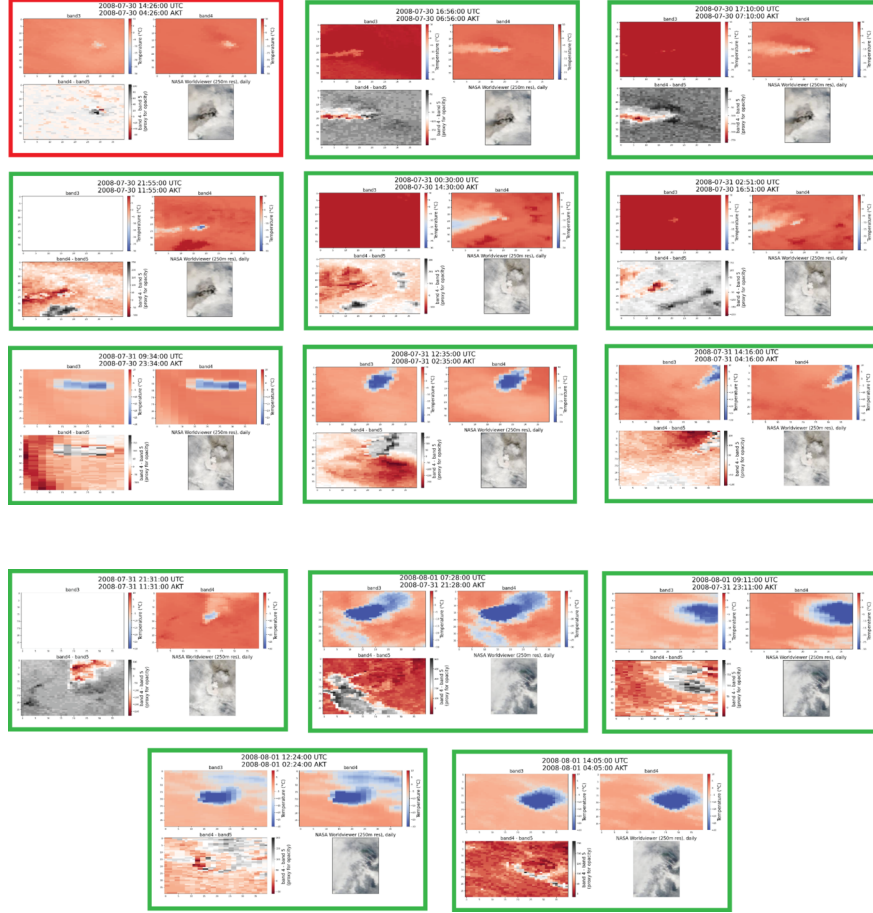


Figure S8. Observations from July 27 to August 1 from the Advanced Very-High-Resolution Radiometer (AVHRR) (bands 3,4,5) (top and bottom-left panels) and MODIS-Terra and MODIS-Aqua corrected reflectance satellite images from NASA Worldview (bottom-right panel). Red frames indicate that no plume is observed, green frames indicate that a plume is observed. These images were analyzed to confirm the plume observations during the middle of the eruption.

S4. Robustness of LPs earthquake rate vs plumes

One of the key findings in this paper is that the bursts of long-period (LP) earthquakes during the middle of the eruption do not coincide in time with observations of ejected plumes (Larsen et al., 2009). We explain this observation by proposing a clog-and-crack mechanism where fluid pressure is low when the vents are open and plumes are coming out but it increases when the vents get clogged either by partial collapse of the conduit or by a higher ash content reducing the pore space. One of the pitfalls of this observation would be that the lack of LP events during the times of mass transfer into the atmosphere is due to an increase in noise (e.g. continuous tremor) or a lack of detectability related to gaps in the data. Therefore, in this section of the supporting information we show that the changes in LP rate during the middle of the eruption (July 26-August 5), when bursts of migrating LPs are observed (see main text), do not depend on either an increase in RMS amplitude or data gaps. Figure S9 shows the 4-hour earthquake rate for LP events during the times of lack of correspondence with plume observations along with the 1-5 Hz average RMS amplitude

measure in two broadband stations (OKFG and OKSO, see Figure 1 in main text) (Figure S9a) and data gaps (Figure S9b). The red curve in Figure S9b is a measurement of percentage of non-usable data, which we define as times when data was simply missing (i.e. gaps) or was corrupted (e.g. electronic artifacts, clipping), for all the stations in the Okmok Volcano network.

As can be seen, neither the average RMS or the percentage of non-usable data explain the lack of detection of LP events during the extraction times (i.e. plumes). Therefore we conclude that the lack of correspondence is due to a physical mechanism rather than an observational artifact.

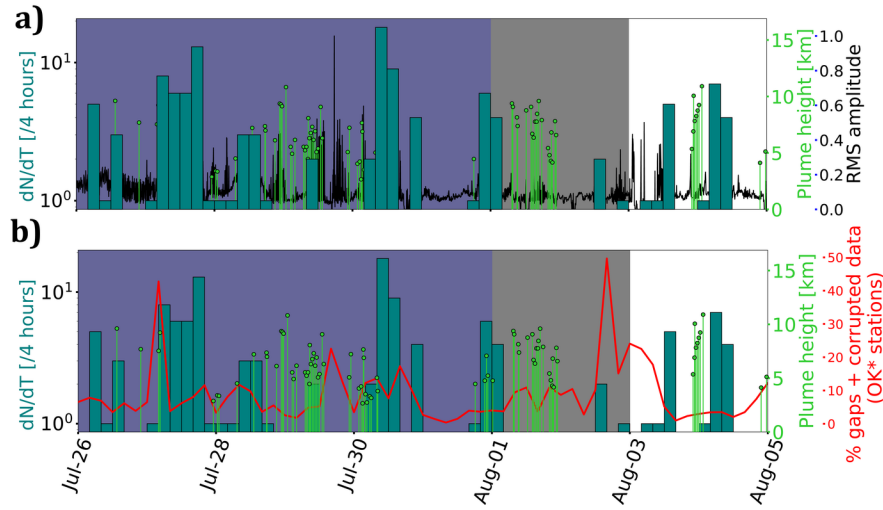


Figure S9. 4-hour seismicity rate for LP events compared to the plume observations (green stems) and the average RMS amplitude in the two broadband stations (OKFG and OKSO) at 1-5 Hz measured every 5 minutes (black curve in panel a) and the percentage of non-usable data in the Okmok Volcano network (red curve in panel b). Neither the RMS amplitude or the corrupted or missing data explain the lack of LPs detection during times of plume observations.

S5. Earthquake clustering

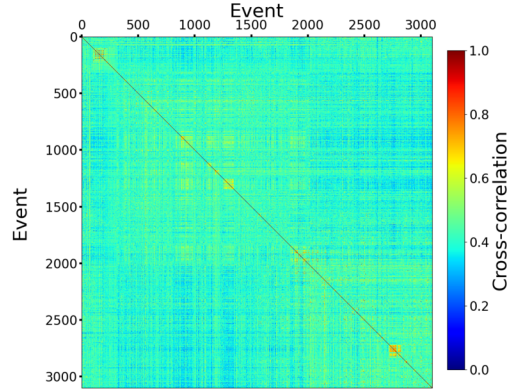


Figure S10. Cross-correlation (CC) matrix with full range of CC values between all pairs of events. Compare this to the colorbar-saturated version in the main text (Figure 9). The events are sorted in time.

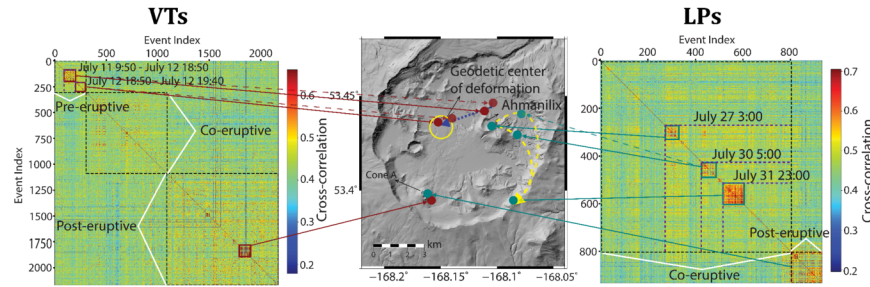


Figure S11. Cross-correlation matrix using a saturated color scale at 3 standard deviations from the mean cross-correlation with the GrowClust catalog. . Compare this to Figure 9 in the main text which used the HypoDD Locations. Dashed arrows point at the centroid of each cluster for the GrowClust relocated catalog when these are more than 1 km away from the centroid given by the hypoDD catalog. Turquoise squares/arrows show LP activity. Red squares/arrows show VT activity. Dashed orange arrow shows the suggested precursory VT migration path toward the deflation source (yellow circle). Dashed yellow arrow shows the co-eruptive LP migration path suggested by the GrowClust catalog and the solid yellow line shows the path suggested by the hypoDD catalog. The events are sorted in time.